Azimuthal anisotropy from eikonal tomography: example from ambient-noise measurements in the AlpArray network

E.D. Kästle [1], I. Molinari [2], L. Boschi [2,3,4] E. Kissling[5] and the AlpArray Working Group

[1]*Institute for Geological Sciences, Freie Universität,* 12249 *Berlin, Germany.* E-mail: *emanuel.kaestle@fu-berlin.de*
[2]*Istituto Nazionale di Geofisica e Vulcanologia, Sezione di,* 40128 *Bologna, Italy*
[3]*Dipartimento di Geoscienze, Universitá degli Studi di,* 35131 *Padova, Italy*
[4]*Institut des Sciences de la Terre Paris, Sorbonne Université, CNRS-INSU, ISTeP UMR* 7193, *F-75005 Paris, France*
[5]*Department of Earth Sciences, ETH,* 8092 *Zürich, Switzerland*

SUMMARY

Ambient-noise records from the AlpArray network are used to measure Rayleigh wave phase velocities between more than 150 000 station pairs. From these, azimuthally anisotropic phase-velocity maps are obtained by applying the eikonal tomography method. Several synthetic tests are shown to study the bias in the Ψ_2 anisotropy. There are two main groups of bias, the first one caused by interference between refracted/reflected waves and the appearance of secondary wave fronts that affect the phase traveltime measurements. This bias can be reduced if the amplitude field can be estimated correctly. Another source of error is related to the incomplete reconstruction of the traveltime field that is only sparsely sampled due to the receiver locations. Both types of bias scale with the magnitude of the velocity heterogeneities. Most affected by the spurious Ψ_2 anisotropy are areas inside and at the border of low-velocity zones. In the isotropic velocity distribution, most of the bias cancels out if the azimuthal coverage is good. Despite the lack of resolution in many parts of the surveyed area, we identify a number of anisotropic structures that are robust: in the central Alps, we find a layered anisotropic structure, arc-parallel at mid-crustal depths and arc-perpendicular in the lower crust. In contrast, in the eastern Alps, the pattern is more consistently E–W oriented which we relate to the eastward extrusion. The northern Alpine foreland exhibits a preferential anisotropic orientation that is similar to SKS observations in the lowermost crust and uppermost mantle.

Key words: Seismic anisotropy; Seismic interferometry; Seismic tomography; Wave propagation; Continental tectonics: compressional.

1 INTRODUCTION

With the availability of very dense seismic network data, array-based surface-wave measurements, such as the ambient-noise technique, as well as array-based tomographic imaging methods have found increased popularity. The eikonal tomography method, so termed by Lin *et al.* (2009) because of its relation to the eikonal equation (e.g. Wielandt 1993), relies on dense array measurements and is based on the direct conversion of phase traveltimes into phase-velocity maps without the need for an inversion. The method has been successfully applied to the USArray using surface wave measurements both from ambient noise and from earthquakes (e.g. Lin *et al.* 2009; Lin & Ritzwoller 2011a) but also on more local scales (e.g. de Ridder & Dellinger 2011; Mordret *et al.* 2013; Xu *et al.* 2016).

In this study we make use of ambient-noise surface-wave measurements from the AlpArray experiment (fig. 1, Hetényi *et al.* 2018) evaluated over 2 yr (2016–2017). It has been shown in various regions that crustal anisotropy can be imaged with ambient-noise techniques (e.g. Lin *et al.* 2009; Fry *et al.* 2010; Gallego *et al.* 2011; Lin & Ritzwoller 2011a; Guo *et al.* 2017). The additional information contained in the azimuthal anisotropy can help to understand the tectonic evolution, because it is sensitive to preferential orientation of structures from the smallest (mineral alignment) to the largest scale (kilometre scale folds and faults, asthenospheric flow field, e.g. Nicolas & Christensen 1987; Kern 1990; Silver 1996). This adds a dynamic component to the observations, linked to temporal variations such as the strain field.

The European Alps are a complex and relatively small mountain belt which was mainly formed by the continental collision of the

European and Adriatic Plate around 35 Ma (fig. 1, Handy *et al.* 2010; Carminati *et al.* 2012, and references therein). The indentation of the Adriatic Plate into the European one led to major crustal reorganizations such as a mantle wedge being pushed to crustal depths in the Ivrea zone (e.g. Malusà *et al.* 2015; Zhao *et al.* 2015) and, in the Neogene, to the sinistral movement along the Giudicarie fault and the exhumation of the Tauern window (e.g. Scharf *et al.* 2013; Verwater *et al.* 2021). The latter was supported by an eastward extrusion of the eastern Alpine units between the Periadriatic Fault in the South and the SEMP fault in the north (Scharf *et al.* 2013). This movement was likely triggered by the northeastward retreating subduction of the last remnants of the Tethys ocean during which the arcuate shape of the Carpathians was formed and the Pannonian basin opened (Handy *et al.* 2014, and references therein). The Carpathians are now almost entirely separated from the Alps by the Pannonian basin and the Vienna basin (Fig. 1). At the junction, the Carpathians bend northeastward around the Bohemian Massif, an area of thick and old continental crust that was amalgamated during the Variscan orogeny (e.g. Schulmann & Gayer 2000; Franke *et al.* 2017). These major changes, first from the continental plate collision and later the large reorganizations at the beginning of the Neogene, severely affected both crustal and mantle structure in the Alpine region. For example, slab break-offs have been proposed at different times and for different parts of the Alps (for a review see Kästle *et al.* 2020). Indications for a slab break-off under the eastern Alps have been found by Qorbani *et al.* (2015) when evaluating the azimuthal anisotropy from SKS splitting data. The pattern of crustal seismicity in the central Alps has been explained with bouyant crustal material that was dragged down by the retreating European slab (Kissling & Schlunegger 2018). Such a process is expected to affect the strain field in the Alps and thus leave an imprint in the crustal anisotropy. Currently, there are, however, hardly any studies that image the anisotropic structure in the Alps at sufficiently high resolution to provide an understanding of how anisotropy links to past and ongoing tectonic processes (Fry *et al.* 2010; Alder *et al.* 2021). With this work we will thus present and discuss eikonal tomography as a potential method to image azimuthal anisotropy at crustal and uppermost mantle level from surface waves. In the following, we will continue previous efforts (Kästle *et al.* 2016) to provide an automated and robust phase-velocity picking algorithm from ambient-noise based Love and Rayleigh waves cross-correlation measurements. The phase-velocity curves are then used to create azimuthally anisotropic maps of the phase-velocity structure by applying the eikonal tomography method. The potential but also the limits of the method that can lead to a significant bias in the amplitudes of the inferred anisotropic field will be discussed. Both methods (phase-velocity picking and eikonal tomography) are made available as Python based tools that are free to use, easy to modify and run platform independent on any machine (supplement).

2 METHODS

2.1 Data preparation and cross-correlation calculation

In this study, we use 2 yr of continuous data recorded at all available AlpArray seismic network stations (permanent and temporary). The data processing is handled with a slightly modified version of the ANTS 2 toolbox (link in acknowledgements), which includes the following steps: (1) removal of time windows after large earthquakes ($M_W > 5.6$), for which the earthquake information is taken from the GCMT catalogue (Dziewonski *et al.* 1981; Ekström *et al.* 2012). The length of the time window to be removed from the record is chosen according to the approximation by Ekström (2001). (2) Local earthquake events are requested via the IRIS catalogue (www.iris.edu) and a time window, a few seconds before the estimated first *P*-wave arrival until all direct signals travelling with velocities 1 km s⁻¹ have passed, is removed. (3) Seismic signals from events that do not appear in the used catalogs and other high-energy sources are removed, applying a filter that compares the signal standard deviation of subsequent time windows according to Boue *et al.* (2013). (4) Cosine tapering, detrending and demeaning of all data. Each window has a maximum length of 1 d. (5) Antialias (lowpass) filter with a cutoff frequency at 1 Hz. (6) Downsampling to 2 Hz. (7) Removal of the instrument response with a water level deconvolution, including a pre-filter (flat between 2 and 200 s, cut-off periods at 333 and 1 s).

From the pre-processed data, cross correlations are calculated between the vertical records (ZZ) of all available stations pairs. Stations pairs with an interstation distance smaller than 20 km are skipped. The data are cut into windows of 1 hr, witch successive windows having an overlap of 60 per cent, each window is cosine tapered (2.5 per cent at the beginning and end of each window) and linear trends are removed. We then apply a Fourier transformation and whiten the signals in the frequency domain by division with the absolute of the spectrum plus a water level for stabilization. From the whitened spectra, the daily cross correlations are calculated and stacked resulting in a total number of 261 388 vertical-component correlations.

2.2 Phase-velocity extraction

From the cross correlations, phase velocities between station pairs are determined by using the zero crossings of the cross-correlation spectra (Aki 1957; Ekström *et al.* 2009; Kästle *et al.* 2016). The method is based on the assumption of a 2-D wavefield (e.g. surface waves) composed of plane waves traveling in random directions. If this wavefield is recorded for a sufficiently long time at two stations, cut into windows, correlated and stacked, the resulting cross-correlation spectrum will resemble a Bessel function (Aki 1957). The argument of the Bessel function depends on the interstation distance times frequency divided by phase velocity, thus, for a given set of these parameters, its zero crossings are known. The phase velocity can therefore be determined from a cross-correlation spectrum by fitting its zero crossings to the ones of the Bessel function. This approach does not rely on the amplitude information of the cross-correlation spectrum which is normally distorted by the variability of energy arriving for different frequencies and by applying the spectral whitening. The cross-correlation spectrum is often affected by noise, inhomogeneous microseismic source distributions and very low energy at the low-frequency end of the spectrum. Consequently, zero crossings may be missed or double crossings appear and it becomes impossible to fit a unique Bessel function to a given spectrum. The non-uniqueness can be partially resolved by restricting the range of allowed phase velocities to realistic values. In the case of Rayleigh-wave phase velocities, extracted from the ZZ cross correlations, we only allow values between 1.5 and 5.0 km s⁻¹ which represent the range of expected phase-velocities for these waves at our periods of interest (2–200 s). The procedure is illustrated in Fig. 2 and consists of the followings steps: (1) cross correlations for which less than 150 d are stacked are discarded; (2) applying a time domain filter that suppresses signals arriving with a velocity below
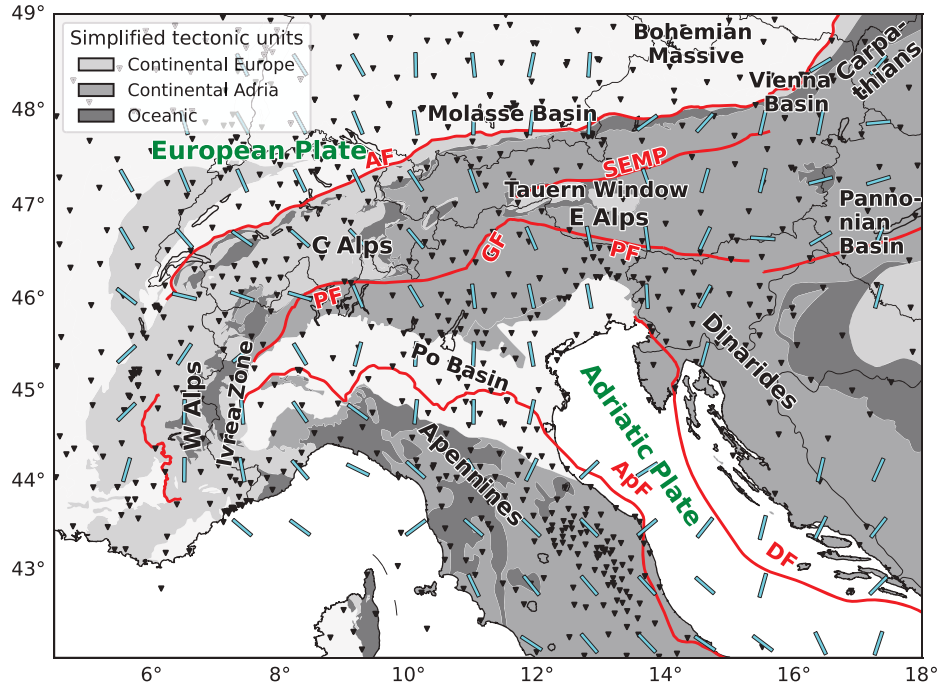
Figure 1. Tectonic overview map showing station locations (black triangles, permanent and temporary AlpArray stations) and a simplified principal stress field (cyan, stress directions averaged in 100 km radius, data set from Heidbach *et al.* 2016). AF, Adriatic Front; ApF, Apenninic Front; DF, Dinaric Front; PF, Periadriatic Fault; GF, Giudicarie Fault; SEMP, Salzach-Ennstal-Mariazell-Puchberg fault. Tectonic units and major lineaments simplified from Schmid *et al.* (2004, 2008) and Handy *et al.* (2010).
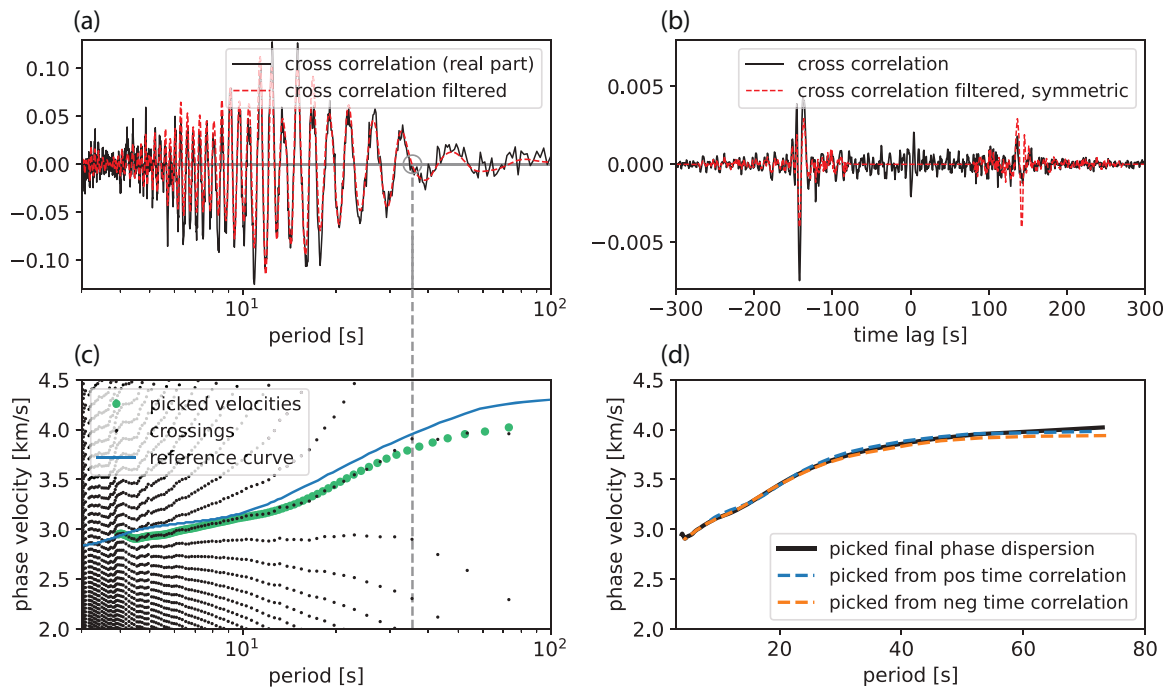

Figure 2. Example of the zero-crossing picking method for the station pair OX.FUSE, Z3.A073A, at an interstation distance of 398 km. Panels (a) and (b) show the vertical component cross correlation in the frequency and in the time domain. The red dashed lines illustrate the effect of the velocity filter between 1 and 5 km s^{-1}. The time domain cross correlation is further symmetrized by discarding the imaginary part of the cross-correlation spectrum. The resulting phase-velocity curve is shown in the bottom panel. (c) shows the phase velocities associated to the zero crossings, exemplarily illustrated by the gray dashed line between panels (a) and (c). Panel (d) shows the good fit of the dispersion curves when only the cross correlation at positive/negative lag times or the symmetric (final) one is used.

1 km s⁻¹ and above 5 km s⁻¹. This results in a smoothed spectrum in the frequency domain; (3) the signals at positive time lags and negative time lags are treated separately and if the picked phase velocities for the two arrivals are too different (mean difference >0.3 km s⁻¹), the whole cross correlation is discarded (eliminates ~20 per cent of the available data); (4) otherwise, the correlation is symmetrized and a final phase-velocity dispersion curve is picked.

The picking procedure itself is similar to the one described in Kästle *et al.* (2016). Each zero crossing in Fig. 2 can be associated with multiple phase velocities as illustrated in Fig. 3. To resolve this ambiguity between parallel branches, a reference curve, for example, derived from a regional average velocity model, is necessary that guides the picking algorithm at the low-frequency end of the spectrum. For low frequencies, the branches are sufficiently far apart, so that a unique pick can be taken. The original procedure of Kästle *et al.* (2016) is modified such that the phase velocities are not picked directly from the zero crossings as this may result in rough dispersion curves or wrong picks in case of noisy data. Instead, an elliptical-shaped area around each zero crossing is defined and an intensity is assigned within this area, ranging from 1, at the location of the zero crossing, to 0, at the boundary of the ellipse (Fig. 3). By summing the overlapping contributions from all ellipses, a smooth intensity field is created and picks are taken where the intensity is maximized. This can be understood as a Kernel Density Estimation (KDE) with a cosine shaped kernel varying between 1 in the centre and 0 at the edge of the ellipse. Size and orientation of the kernels/ellipses have to be chosen carefully, as the *x*- and *y*-axis have very different values and as the branches become narrower with increasing frequency. We deal with this issue by making an estimate of the *y*-axis distance between branches and the *x*-axis spacing between subsequent zero crossings. The estimate is based on the reference curve and on previous picks, which also controls the orientation of the elongated axis of the ellipses. Our implementation allows to easily adjust the picking behaviour by modifying the kernel sizes depending on the application and data quality. The full code is available online and in the supplement to this paper. With the applied criteria, we obtain a total of 164 116 phase-velocity curves from ZZ correlations. The described program can also extract phase velocities for the horizontal component correlations (TT, RR), in this case the second order Bessel function term is taken into account as discussed in Kästle *et al.* (2016).

2.3 Isotropic eikonal tomography

The procedure described in the following is available as a Python tool from the supplementary material to this paper. We adapted this tool from previous works of Lin *et al.* (2009) and Lu (2019). The eikonal tomography method was originally proposed by Lin *et al.* (2009) and is based on the eikonal equation (e.g. Shearer 2009),

$$\frac{1}{c^2} = | \nabla T |^2, \tag{1}$$

which relates the phase velocity *c* to the gradient of the traveltime field ∇T, valid at the high-frequency limit. Lin *et al.* (2009) argue that the method takes ray bending into account and, despite the high-frequency assumption, approximates the influence of the finite-frequency kernel. It has been shown for ambient-noise applications that the typical error introduced by this high-frequency approximation is below 2 per cent of the mapped velocity variations (Lin & Ritzwoller 2011a; Mordret *et al.* 2013). The application of this method is straightforward, the traveltimes from one arbitrarily chosen central station to all other stations are interpolated onto a

regular grid. By taking the inverse of the gradient of this traveltime field, the distribution of velocities is obtained (eq. 1, Fig. 4). This procedure is repeated for all possible central stations. The final, isotropic map is calculated from the average of the ensemble of maps. In general, the method requires no regularization, compared to well-established linearized inversion approaches that apply damping or smoothing (e.g. Boschi & Dziewonski 1999). However, the method of interpolating the traveltimes from the single station measurements to a regular grid can have an important influence on the result. Small errors in the traveltimes can lead to strong variations in the gradient field which, by taking the inverse of these spurious gradients, may cause large velocity jumps. It is therefore necessary to apply an interpolation scheme that produces sufficiently smooth traveltime fields, to compensate measurement errors, without over-smoothing and thus loosing information. In practice, previous works (Lin *et al.* 2009; Lin & Ritzwoller 2011a; Mordret *et al.* 2013) have often applied the spline-in-tension method (Smith & Wessel 1990). However, we prefer to use (smooth) radial basis splines (a comparison of four different interpolation schemes is shown in Fig. S2). For the spline-in-tension method, the interpolated surface is required to pass through all nodal points (i.e. stations where a traveltime has been measured), while the tension parameter can suppress spurious oscillations between points (Smith & Wessel 1990). With the use of smooth radial basis splines, we have the additional option to obtain a smooth surface without the necessity to fit all nodal points which can be advantageous in the case of measurement errors. Our tests indicate that the difference from the chosen interpolation method is relatively small at most periods, if spurious velocity spikes are removed [step (iv) below] before all models are stacked (Fig. S2). To be as independent as possible of user-defined regularization parameters, the smoothing parameter for the interpolation is only controlled by the obtained velocities. The user has thus to define a threshold given in terms of deviation from the mean velocity, which is more intuitive and related to a physical property of the medium. The procedure is illustrated in Fig. 4 and consists of the following steps:

(i) A central station is chosen and all phase-traveltime measurements between this station and all other stations are extracted from the data set. Measurements from stations that are closer than one wavelength from the central station are ignored. We set a minimum threshold of 10 measurements.

(ii) An initial interpolation where the traveltime surface passes through all nodal points reveals areas of strong curvature. Traveltime measurements at stations that are associated with a curvature that deviates by more than a threshold of two standard deviations from the mean are considered outliers and are discarded. This rejects about 5 per cent of the measurements.

(iii) The smoothing parameter of the interpolation starts at zero (no smoothing) is iteratively increased until all velocities are below a user-defined threshold (in this work, three times the regional average velocity). If the interpolation grid is finer, it will automatically lead to a larger smoothing parameter, as a rough grid causes implicit smoothing by taking the blockmean of all station measurements within one grid cell.

(iv) Regions of the velocity map that show velocities that deviate by more than a second threshold (in this work, 50 per cent) from the average velocity are removed from the map. This removes on average less than 1 per cent of the mapped area.

(v) Regions of the velocity map that are outside the convex hull defined by the station locations, as well as regions that are too far
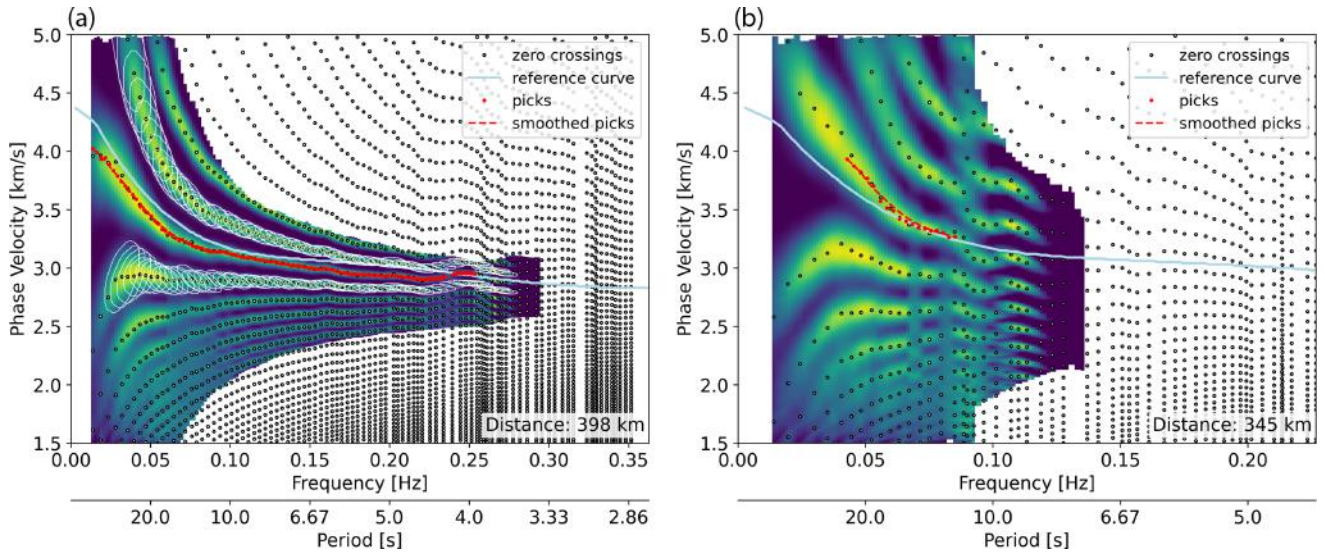
Figure 3. Procedure to extract phase velocities from the zero crossings of the cross correlation spectra. For each zero crossing, a multitude of Bessel functions can be found that pass through it, resulting in the ambiguity of the subparallel branches. The correct branch is chosen by starting the picking procedure close to the reference curve, at the low-frequency end. The algorithm stops automatically when the data quality is too bad to choose a good next pick. The background colours scale with the number of nearby zero crossings and are controlled by the white ellipses around each zero crossing. For better visual clarity, only the ellipses along two branches are shown in panel (a). The zero crossings in panel (a) are from the cross correlation in Fig. 2 (OX.FUSE, Z3.A073A). Panel (b) shows the same for a station pair with lower data quality (SK.MODS, Z3.A359A). At the low frequency end, the branches are too far from the chosen reference curve so that the choice of the right branch is ambiguous. The picking algorithm starts thus at higher frequencies. Because of jumps in the crossings, the picking is not completed and the result discarded.
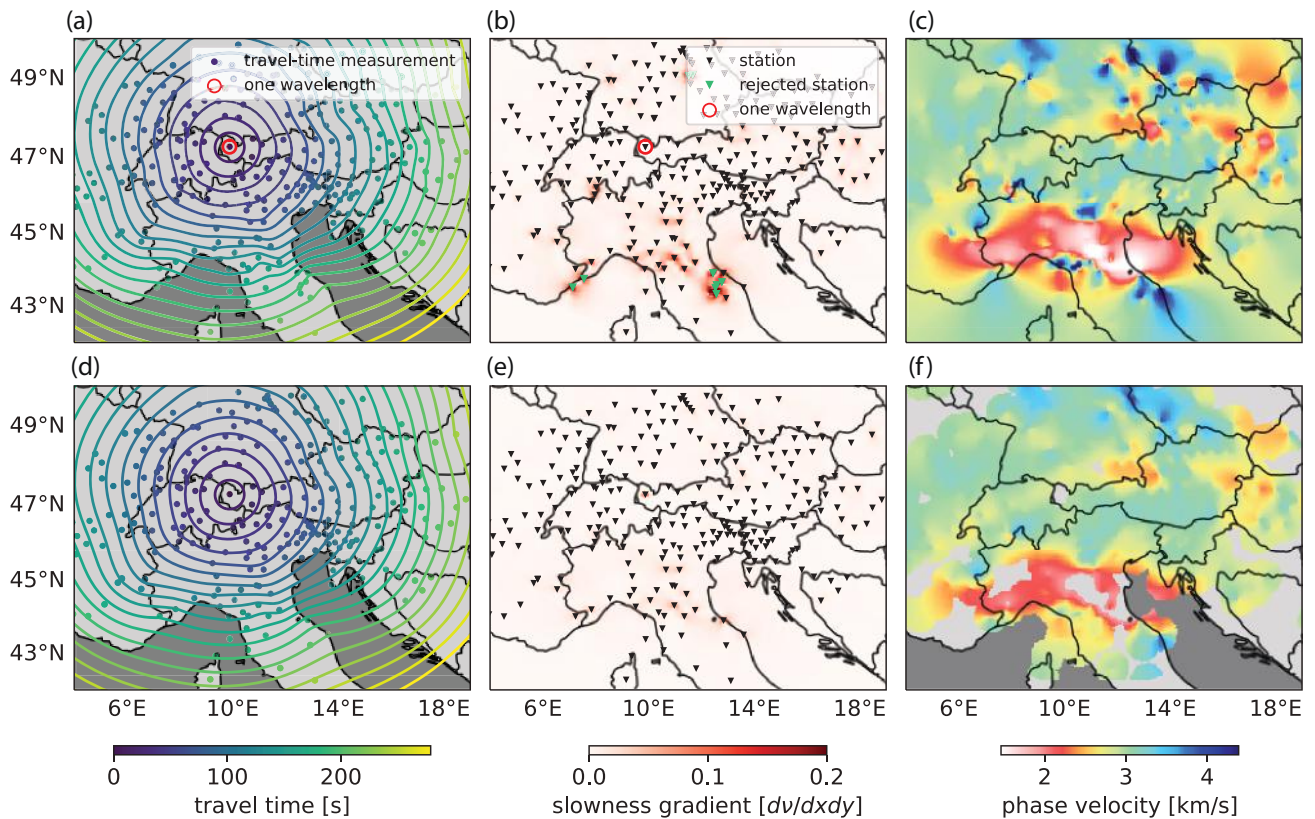

Figure 4. Example of the eikonal tomography procedure for a single central station for data measured at a period of 6.5 s. Panels (a)–(c) show phase traveltime measurements, interpolated traveltime field, curvature of the traveltime field and the deduced phase velocities, all before any data rejection or interpolation smoothing has been applied. Panels (d)–(f) show the same after processing. The final phase-velocity map is created by taking the processed maps (f) and stacking them for all available central stations. Grey parts of the map indicate that measurements in these areas have been rejected, because the closest station is too far away, the azimuthal coverage is bad or there are too few values to obtain a stable average velocity estimate.

away from the next station are removed. We choose a distance limit of 50 km at short periods, and one wavelength at long periods.

(vi) Steps 1–5 are repeated for all available central stations.

(vii) At all grid points, the mean and the standard deviation of the phase-velocities is calculated. Velocities that deviate by more than two standard deviations from the mean are rejected.

(viii) The final phase-velocity map is obtained by splitting the mapped phase velocities into azimuthal bins and taking the mean of the phase velocities in each bin. Areas where the gap in azimuthal coverage is greater than 60° and where less than 50 phase-velocity values are averaged are rejected. Secondly, the contributions of all bins are averaged for each grid cell. This two-step averaging procedure makes sure that the average is not biased by the number of measurements from different azimuths.

The example in Fig. 4 shows how the procedure removes roughness in the traveltime field and very high amplitudes in the phase-velocity map. It is observable that the highest variance in the traveltime field appears at large distances from the central station, leading to spurious phase velocities. We checked that this is independent of the chosen interpolation method and interpret it as an effect of increasing measurement uncertainty with distance for the given data set and also increasing distortions of the traveltime field by velocity variations within the medium. The effect is especially strong around the shown period of 10 s and decreases towards both shorter and longer periods. We also achieve good results for the eikonal tomography method if we reject measurements that are further away than about 300 km from the central station. In this case, the interpolation smoothing becomes unnecessary (not shown here). However, because this leads to a rejection of a very large part of the data set, we decide not to apply an upper distance limit.

2.4 Anisotropic eikonal tomography

As shown by Lin *et al.* (2009), the eikonal tomography method can be used to determine the azimuthally anisotropic velocity structure. For each central station, we can estimate not only the velocity in each cell of the interpolated grid, but also the direction of the traveltime gradient, that is the direction of propagation. With this information it is possible to determine azimuthally dependent velocity variations by fitting them to the following equation for slightly anisotropic media (Smith & Dahlen 1973) to which we added a Ψ_1 term, similar to previous works Lin & Ritzwoller (2011a):

$$c(\omega, \psi) = c_0(\omega)(1 + A_1 \cos(\psi - \Psi_1) + A_2 \cos(2(\psi - \Psi_2))$$
$$+ A_4 \cos(4(\psi - \Psi_4))), \tag{2}$$

where $c(\omega, \psi)$ is the phase velocity, depending on the angular frequency and the azimuth, c_0 is the isotropic velocity and A_1, A_2 and A_4 are the amplitudes of the Ψ_1, Ψ_2 and Ψ_4 components. In practice, values of A_x and Ψ_x are found by optimizing the least-square fit to the c values, identified as described above. The Ψ_1 term is non-physical, because it means that two waves propagating in opposite directions have not the same velocity which violates the reciprocity of the wave equation. However, Lin & Ritzwoller (2011b) have shown that the azimuthal velocity measurements can be biased in such way that there appears a Ψ_1 periodicity. Inclusion of the Ψ_1 term can thus avoid tradeoff with the Ψ_2 and Ψ_4 components and serve as an indicator for biased measurements (discussed below).

It can be difficult to get stable estimates of the anisotropy, because the expected amplitude of the azimuthal phase-velocity anisotropy

is in the range of 0–3 per cent (e.g. Fry *et al.* 2010) and therefore close to the expected range of measurement errors deduced from the mapped standard deviations and from previous works (1–2 per cent, Kästle *et al.* 2016). Additionally, the sensitivity of the eikonal tomography method to small traveltime errors can yield very large velocities at some locations and travel azimuths. It is therefore necessary to average over a larger area, which has already been shown in previous works (Lin *et al.* 2009; Lu 2019), while taking care not to lose too much information in regions where the fast axis direction shows strong lateral variations. After some testing, we found a good compromise by averaging over circular regions of 30 km radius and summarizing the azimuths of the velocity measurements into bins of 15°. The anisotropic parameters are only determined at locations where the total azimuthal coverage is more than 300°. In each cell, the isotropic phase-velocity is subtracted before performing the regional averaging and fitting procedure to minimize trade-off effects between isotropic velocity variations within the circular region and the anisotropic parameters.

3 SYNTHETIC EXAMPLE

We set up a test model as shown in Fig. 5 and calculate synthetic traveltime data using the fast marching method (FMM) so that the rays are bent according the the velocity structure. The isotropic model is based on a satellite image which serves as approximation to a characteristic earth structure with different anomaly sizes and shapes. For this example, we use the same path coverage as in the measured data set comprising ∼71 000 measurements between station pairs resulting in phase-velocity models from 656 different central stations. An error is added to the synthetic data, defined in terms of velocity with a standard deviation of 0.02 km s⁻¹, which corresponds to a relative velocity error of 0.5 per cent. This means that the absolute traveltime errors are larger for large interstation distances, as is expected from the attenuation and the subsequently lower signal-to-noise ratio over large distances. The same processing steps and parameters as listed above are used to recover the model. The smoothing parameters in the interpolation was always zero as the velocity error never exceeded the threshold for the synthetic measurements [step (iii) in Section 2.3].

The large scale features of the example model are well recovered, smaller features are smoothed out leading to a general reduction of the anomaly strength, especially for smaller structures. Structures of sizes below about 30 km are not being recovered. The smoothing is caused by two related factors: (1) the traveltime field from each central station is only sampled at a subset of the stations shown in Fig. 5(c) and is therefore missing details and (2) the incomplete reconstruction of the traveltime field causes errors in the velocity field (see blue dots Fig. 5d) that lead to a smooth model when averaged over the models from all available central stations. The smoothing effect is also seen in the anisotropic parameters between patches of identically oriented anisotropy, as well as at the border of the patches.

In a next test, we check how stable the eikonal tomography works in the presence strong velocity heterogeneities. We do so by increasing the amplitude of the isotropic velocity variation while keeping the anisotropic pattern identical to the one already shown in Fig. 5. The resulting maps in Fig. 6 show that the quality of the recovered isotropic model remains almost constant, illustrated by the stable relative errors (a relative residual of 10 per cent for the 15 per cent—anomaly model means an absolute error of 1.5 per cent, i.e. 0.06 km s⁻¹). While the relative isotropic velocity residual does
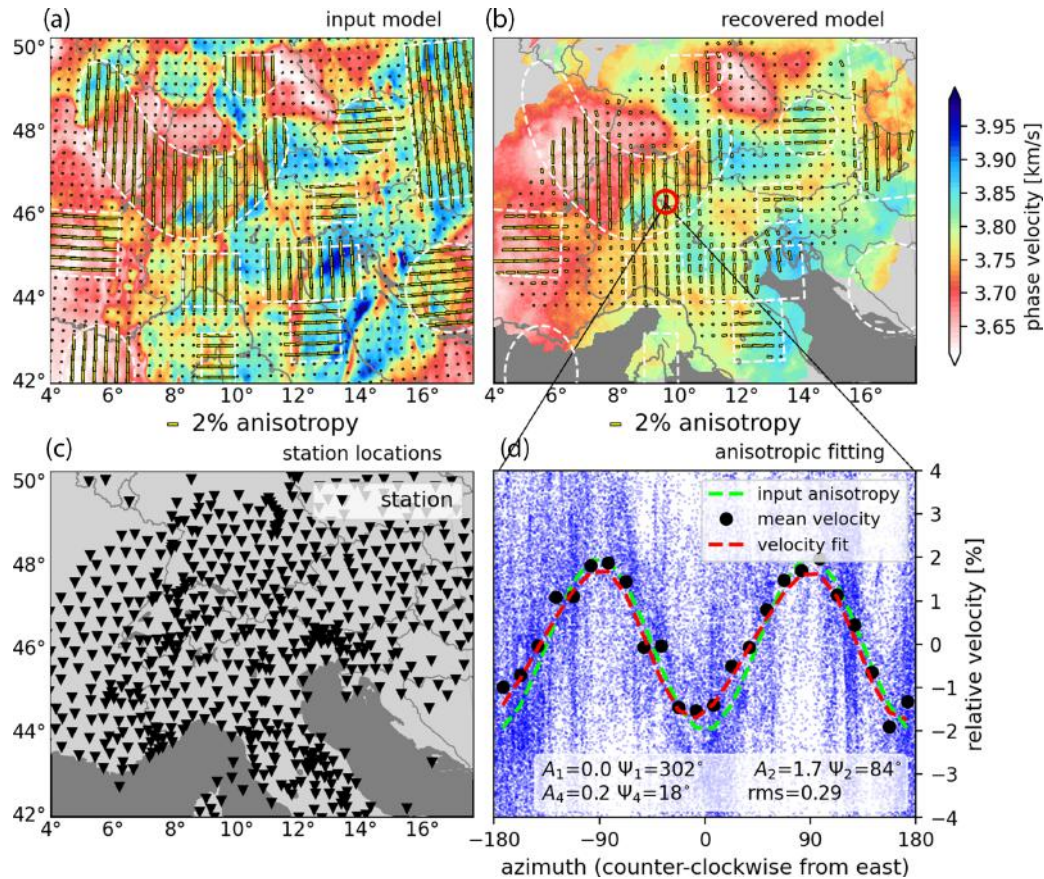
Figure 5. Synthetic test for an isotropic model (transformed from satellite image, credit: ESA, CC BY-SA 3.0 IGO) overlain by patches of either N–S oriented, E–W oriented anisotropy (2 per cent) indicated by yellow bars. The data coverage is identical to that of the real data set at 6.5 s period with the station configuration shown in (c). Panel (a) shows the synthetic input model, (b) the recovered model. The red circle indicates exemplarily the 30 km averaging radius for the determination of the anisotropic parameters. The red bar highlights one example location for which the fit to the anisotropic parameters is shown in (d). The blue dots in the background give the individual measurements within the 30 km averaging radius.

not change significantly with the anomaly strength, there is a clear dependence on the anisotropic residual. For the 5 per cent model in Fig. 6, the anisotropic residual is relatively small and is visible mostly inside the patch regions with the same orientation as the input anisotropic direction. This indicates that the recovered anisotropy points in the right direction but has a smaller amplitude than the one in the input model. The residual tends to be larger for small patches and close to the model boundaries. An additional smoothing effect in the anisotropic structure can be explained by the fact that our approach averages measurements inside circular regions of 30 km radius for the determination of the anisotropic parameters. For higher isotropic anomalies (15–25 per cent), the anisotropic fast axis orientation is still mostly correct within the patches, but a spurious signal appears outside these regions. It becomes clear that strong isotropic velocity variations introduce a bias in the anisotropic model.

3.1 Anisotropic bias

To better understand the source of this anisotropic bias and how it would affect the results for the Alpine models, a synthetic test with a purely isotropic velocity model, taken from the real-data models (shown below) is implemented (Fig. 7). The velocities in this example vary by –30 per cent to +16 per cent from the mean velocity.

The very slow velocities are related to the thick sedimentary basin in the Italian Po plain. The synthetic traveltimes are modeled with a finite difference solver (Devito: Luporini *et al.* 2018; Louboutin *et al.* 2019) using a source wavelet with a dominant period of 6.5 s so that we can include finite frequency effects and reflections. The phase traveltime is measured in the frequency domain from the phase of the cross-correlation function between source signal and the signal at the receiver locations. The recovered, final model in Fig. 7(b) shows strong, spurious anisotropy with amplitudes of more than 5 per cent. The areas where the anisotropic bias is most prominent coincide with areas where the traveltime field is strongly curved and concave shaped. In this example, no error is added to the data and the data coverage is idealized with all recorders active for all possible central stations (station locations in Fig. 5c). No data rejection based on local strong velocity variations, as we did in Fig. 6, is performed: in the previous tests, the areas in the seas and close to the model boundaries were rejected because of bad station and bad azimuthal coverage. The spurious anisotropy seems to be less pronounced when the azimuthal coverage is good, but even in regions with perfect coverage (low velocity basin in southern Germany and directly north of the Po basin) the bias is still significant (2–3 per cent).

The phase-velocity map for the single-central-station example in Fig. 7(c) shows that there are significant errors in the recovered velocities, most prominent behind low-velocity zones. One reason for
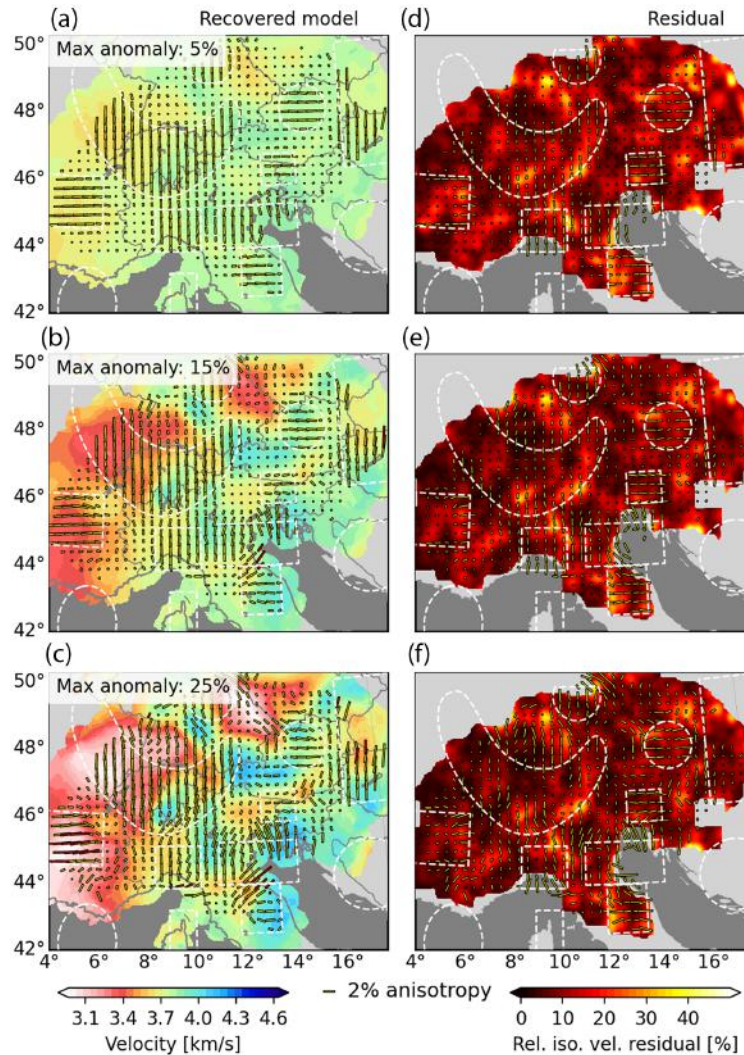
Figure 6. Synthetic tests to illustrate the effect of strong isotropic velocity heterogeneities. The input model for these tests is the same as shown in Fig. 5(a), however, the maximum isotropic velocity anomaly varies from ± 5 per cent [(a), identical to Fig. 5] over ± 15 per cent (b) to ± 25 per cent (c). The strength and pattern of the anisotropy is identical between tests. Panels (d)–(f) give the isotropic velocity difference as colour image and anisotropic residual calculated as vector difference. The isotropic residual maps are slightly smoothed for visual clarity. White dashed lines indicate the location of the anisotropic regions in the input model (Fig. 5).

these artefacts is the occurrence of a secondary wave front down-stream from the sedimentary basins (Feng & Ritzwoller 2017). The first wave front results from the signals traveling around the low-velocity area deforming it to a concave shape. The second wave front is caused by the slower propagation velocity inside the basin. The basin itself acts like a lens that focuses the waves, therefore it is possible that the secondary wave package may have a higher amplitude. Typically, first and secondary waves are not clearly sep-arated in time and will thus interfere (Fig. S4). The effects of slow sedimentary basins on wave propagation angles and amplitudes is discussed in detail in Feng & Ritzwoller (2017). Another effect is caused by back scattering which leads to an undulating phase error (and consequently velocity error) with a $\lambda/2$ periodicity (i.e. wave-length $\lambda \approx 20$ km at period 6.5 s) as described in Bodin & Maupin (2008); Lehujeur & Chevrot (2020). The station sampling distance in Fig. 7 is larger than this periodicity, thus making it hardly visi-ble, but the effect can be seen at longer periods and for very dense sampling examples (Figs S5–S9).

Lin & Ritzwoller (2011b) study in detail the bias in anisotropy from inhomogeneous media when applying eikonal tomography to data from the USArray. The typical station spacing is ∼70 km in USArray and ∼50 km in AlpArray which gives a comparable setup for testing. They mainly attribute the bias to finite frequency effects causing backwards scattering in the vicinity of the receiver locations (mostly responsible for a bias in the Ψ_1 anisotropy) and to wave front healing (Nolet & Dahlen 2000) due to the large size of the sensitivity kernels (responsible for a bias in the Ψ_2 anisotropy). Both Bodin & Maupin (2008) and Lin & Ritzwoller (2011b) find that the bias becomes stronger with increasing velocity contrast, as is the case in our study.

This class of errors from wave interference affect the phase-velocity measurements directly. It could be reduced by picking first (direct) arrival times in the time domain which would be valid for our synthetic test where the source is almost perfectly monochro-matic (Fig. S4). Preliminary tests show that using only the first-arrival traveltime field can indeed reduce the mapped artefacts
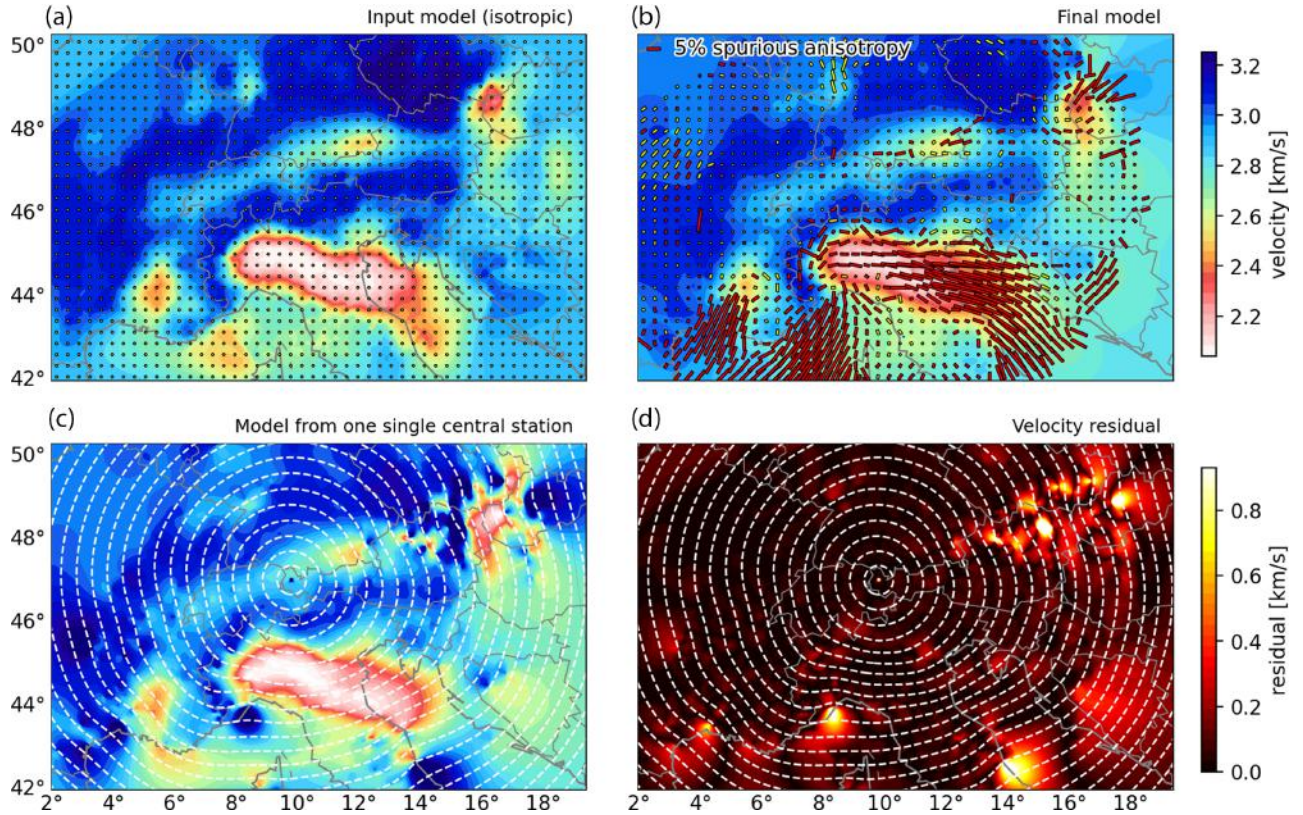
Figure 7. Synthetic test with input model taken from the real data model at 6.5 s. The dominant period for the source signal is chosen accordingly. For the single station example in (c), the same central station as in Fig. 4 is used. In this idealized example, the traveltime field is recorded at all station locations that are shown in Fig. 5(c). The final model in (b) is derived from the ensemble average of all individual single-central-station models. The bars indicate the anisotropy. Red/yellow colour of the bars indicate whether the standard deviation of A_2 (eq. 2) is above/below 0.5. The velocity residual in (d) gives the difference between the models in (c) and (a). White dashed lines indicate the iso-contours of the traveltime field.

(Figs S5–S9). Realistic applications, however, typically deal with dispersive waves and make use of a frequency domain approach to determine phase traveltimes, as for example the FTAN or the Bessel function method described in the previous sections where the entire wave train is taken into account. More than that, if direct and scattered wave packages are too close it becomes difficult or even impossible to isolate the first arriving wave.

The errors related to finite-frequency effects in the recovered velocity field can be better understood in the context of the eikonal equation (eq. 1) that is only valid for smoothly varying media and approximately plane waves (e.g. Wielandt 1993). Eq (1) is a simplification, derived from a Helmholtz representation of the wave equation, in which the amplitude term has been neglected. The full equation reads (Wielandt 1993):

$$\frac{1}{c^2} = |\nabla T|^2 - \frac{\nabla^2 A}{\omega^2 A}, \quad \nabla^2 = \frac{\partial^2}{\partial x^2} + \frac{\partial^2}{\partial y^2}, \tag{3}$$

where A is the amplitude of the wavefield. In terms of Wielandt (1993), the application of the eikonal equation leads to the dynamic phase velocity, not the medium phase velocity which can only be obtained when the amplitude distribution is taken into account (even then an error remains as shown by Friederich *et al.* 2000). The curvature of the wavefield from the point source in Fig. 7 causes only a relatively low error (<0.1 km s^{-1}), but other effects such as wave focusing in low-velocity zones have a more severe influence (Figs S5–S9). The influence of the amplitude term has been studied in several previous works (Bodin & Maupin 2008; Lin *et al.* 2009; Lin & Ritzwoller 2011a; Lehujeur & Chevrot 2020) and it has been

proposed that it becomes negligible at short periods (increasing ω in Eq. 3), for example, below 1 s for the local data set of Mordret *et al.* (2013) or below 40 s for the western part of the USArray data in the work of Lin & Ritzwoller (2011a). Our tests confirm that at long periods much larger portions of the map are biased if the amplitude correction is omitted (for a long period example see Figs S8–S9). Specifically, the $\lambda/2$-periodic phase bias is strongly period-dependent and becomes larger at long periods.

Our tests indicate, however, that also in the short-period (6.5 s) finite difference simulation (finite frequency) and the FMM simulation (infinite frequency) a significant bias in the Ψ_2 anisotropy appears. In both cases, effects such as wave front healing should play only a minor or no role. At high frequencies, the observed bias is mainly controlled by the incomplete reconstruction of the traveltime field by only being able to sample it at the receiver locations. If the traveltime field is strongly distorted, as expected behind strong velocity heterogeneities, extremely dense sampling would be necessary to be able to properly recover it. Typically, this is not the case, resulting in a smoothed version of the traveltime field and thus a phase-velocity bias that is dependent on the azimuth of the wave propagation with respect to the location of the anomaly. The infinite frequency tests (FMM) in Figs S5–S8 show that in case of perfect sampling and if no finite-frequency effects appear the recovered phase-velocity field is almost identical to the input model, as expected. The only remaining artefacts appear in narrow stripes, where the size of the grid cells is larger than the curvature of the traveltime field, and thus the estimation of the traveltime gradient fails. For a stable gradient estimate, the wave front has to

be approximately plane in the area covered by the gridpoint and its four neighbor points used to calculate the gradient. To prove the important influence of the traveltime field sampling in the eikonal tomography method, we have repeated the test shown in Fig. 7 calculating synthetics with the FMM method, that is no finite-frequency effects such as back-scattering, secondary wave fronts, etc. appear. The resulting anisotropic bias is, however, almost identical to the one shown in the finite-frequency simulation (Figs 7, S10–S11). From this we conclude that at short periods, finite-frequency effects are indeed negligible as proposed by Lin & Ritzwoller (2011a) or Mordret *et al.* (2013), but the wavefield undersampling becomes the dominant factor. Short periods are in this context to be understood as relative to the interstation spacing and depending on the complexities of the traveltime field caused by the velocity heterogeneities. The bias from incomplete traveltime sampling can affect the Ψ_1, Ψ_2 and Ψ_4 anisotropic components alike, it is therefore recommendable to model all of them to avoid for example wrong mapping of a spurious Ψ_1 component into the Ψ_2 anisotropy (Lin & Ritzwoller 2011b).

Different from the finite frequency effects that directly bias the measured phase-velocities between station pairs, and thus will affect also other tomographic methods, the issue of the incomplete traveltime field sampling is unique to the eikonal tomography method. The bias from the undersampled traveltime field may be partially mitigated by choosing a different interpolation scheme, however, with the herein discussed methods, we did not note a significant difference.

3.2 Addressing the Ψ_2 bias

In the isotropic phase-velocity maps, most of the discussed bias cancels out by azimuthal averaging. This has been shown analytically for the finite-frequency effects by Lehujeur & Chevrot (2020) and is also suggested by our tests that show a relatively stable isotropic error with increasing velocity anomalies (Fig. 6). However, for the estimation of the azimuthal anisotropy, the contributions from different azimuthal directions need to be treated separately, thus a bias remains. Bodin & Maupin (2008) and Lin & Ritzwoller (2011a) already indicated that including the amplitude term from eq. (3) can significantly reduce the influence from the discussed finite-frequency effects which we confirm in our tests shown in Figs S5–S8. However, a bias will remain, since also the Helmholtz equation is only approximately valid for surface wave propagation in a laterally heterogeneous medium (Friederich *et al.* 2000; Lin & Ritzwoller 2011a). We will not discuss this option in detail, because we estimate it to be unfeasible for typical ambient-noise applications for two main reasons: amplitude measurements from ambient noise are difficult because of issues such as non-uniform source distribution or typical non-linear pre-processing steps that affect different station pairs and time windows differently (e.g. Fichtner *et al.* 2020). More important, however, is the issue of interpolating the strongly varying amplitude information from the station locations onto a dense, regular grid, necessary to calculate the Laplacian of the amplitude field (eq. 3). In our synthetic example at 6.5 s period, we observe an increase in the wavefield amplitude by a factor of 4 in a very narrow stripe that is caused by the interfering wavefields, refracted from the strong velocity contrasts in the model (Fig. S6). In our tests, we are only able to record and properly correct for the amplitude effect if we have 'perfect' sampling, that is an extremely dense distribution of stations with a subwavelength spacing which is unrealistic in most real applications at short periods. Otherwise, the amplitude

field is smeared out or distorted and cannot be used to correct the dynamic phase velocity. Finally, the incomplete reconstruction of the traveltime field poses an even more important source of bias at short periods that cannot be addressed by the amplitude correction.

An alternative to correcting the velocity bias is removing measurements in the map where the traveltime field is strongly curved and thus violates the plane-wave assumptions made in eikonal tomography method (e.g. Mordret *et al.* 2013). The mapped region rejected by this approach changes with different central stations and at short periods only small areas need to be removed thus making it necessary to remove only a few percent of the measurements and still being able to recover the entire region in the ensemble average. This approach works very well in our tests where we have a perfectly dense station distribution (not shown here for the sake of brevity). However, in the case of realistic station distributions, as shown for example in Fig. 7, the regions of highly curved traveltime become smoothed out and cannot be properly identified anymore thus making this approach ineffective.

Lin & Ritzwoller (2011b) propose that the presence of the non-physical Ψ_1 anisotropy may be used as indication of the presence of a bias in Ψ_2. In Fig. 8 we check for a spatial correlation of the bias in with the the Ψ_1 intensity, as well as with the velocity gradient and the uncertainty in the Ψ_2 amplitudes (i.e. std A_2). We find that in all three cases the spatial correlation is weak such that it is not straightforward to filter out biased anisotropic measurements using these three parameters as proxy. The closest spatial correlation is found with the uncertainty in A_2 which we calculate from the covariance of the least-squares fitting procedure to eq. (2). We will reject measurements where the standard deviation of A_2 is greater than 0.5. This value is based on the synthetic test results presented in Figs 6 and 7(b) (see red bars). From the discussion here it is clear that the A_2 standard deviation is only a proxy but no guarantee that all biased anisotropic measurements are excluded. For example, not all of the spurious anisotropy shown in Fig. 6 is also related to areas above the threshold of 0.5 which would get rejected by this approach.

4 RESULTS FOR THE ALPARRAY DATA SET

We apply the eikonal tomography method to the presented AlpArray data set and extract azimuthally anisotropic maps at periods between 3 and 80 s (Fig. 9). We only show isotropic velocities in regions where we have enough values for the averaging procedure and with good azimuthal coverage (see list in Section 2.3), the remaining parts are greyed out. The same applies for the anisotropic parts of the map. We additionally use the uncertainty in the anisotropic intensity, A_2, to identify regions where the anisotropic fast axes are likely biased. We shows these measurements in grey as opposed to the remaining areas that are below this threshold, coloured in yellow in Fig. 9. The comparison of the potentially biased anisotropic areas of the maps with the results of the synthetic test in Fig. 7 reveal that the anisotropic bias is mostly an issue in and around areas of very slow phase velocity. The anisotropic fast axes strengths and directions that are identified as biased follow a similar pattern as in the synthetic test: the fast axes align with the shape of the low velocity anomalies, parallel to the elongation axis within the low velocity areas and curving around the edges, that is parallel to the boundary of the velocity contrast. The uncertainty in A_2 is lowest around 20 s period and increases both towards shorter and longer periods. However, the analysis of the A_2 standard deviation can only serve as a proxy for biases anisotropic measurements, there are also
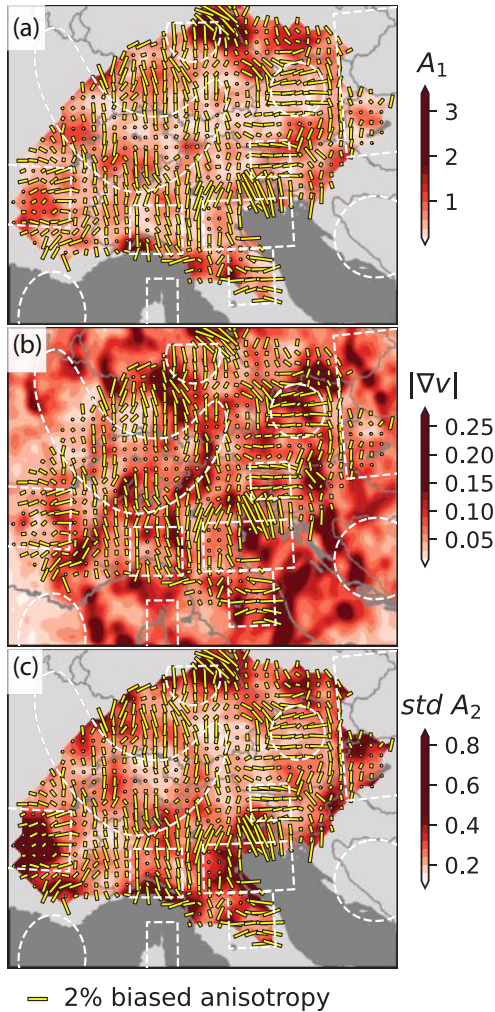
- 2% biased anisotropy

Figure 8. The anisotropic bias presented in Fig. 6 (f) (±25 per cent isotropic velocity variation) is compared to three different parameters: (a) to the strength of the Ψ_1 anisotropy, (b) to the gradient of the velocity field calculated from the input model and (c) to the standard deviation of A_2 (amplitude of the Ψ_2 anisotropy; its standard deviation can be calculated from the fitting procedure to eq. 2). A weak spatial correlation between the biased anisotropy and the strength of all three chosen parameters can be seen.

other factors that influence the uncertainty, such as errors in the measured phase traveltimes. Some regions where the anisotropic fast axis is biases may not be identified at all as can be seen from the test in Fig. 8.

For each map shown at a certain period, we give a depth range which we derive from the calculation of sensitivity kernels based on the model of (Kästle *et al.* 2018, fig. S1). The min/max values of the depth ranges are chosen so that, on average, 50 per cent of the surface under the sensitivity kernel lies within that range. Low velocity areas, such as the sedimentary cover in the Po-basin or the thick crustal root underneath the Alps, shifts the peak sensitivity to shallower depths. For example, in the map at 30 s in Fig. 9, velocities and fast axis directions under the Alps and Apennines are most influenced by crustal structures, while outside, they are mostly influenced by mantle features. The isotropic structures are very similar to the ones obtained by other inversion approaches previously applied in the Alpine area (e.g. Kästle *et al.* 2018; Lu *et al.* 2018). The mapped velocities are smoother compared to these previous

studies with slightly reduced anomaly amplitudes compared to a linearized inversion approach (Fig. S2). This observation is, however, strongly dependent on the chosen thresholds in the eikonal tomography method (see Section 2.3) and the regularization parameters in the linearized inversion.

5 DISCUSSION

5.1 Variance reduction

The variance reduction serves as a measure to compare the final models' data fit to the fit to a constant velocity model. We define it as

$$\text{variance}_\text{r}\text{eduction} = 1 - \frac{\sum \left(t_i^\text{mod} - t_i^\text{obs}\right)^2}{\sum \left(t_i^\text{ref} - t_i^\text{obs}\right)^2}, \quad (4)$$

where t_i is the traveltime between the ith station pair in the observed data (obs), in the final phase-velocity maps (mod) and in the constant velocity 'reference model' (ref). The variance reduction gets closer to 1 as the fit improves. The traveltime in the final phase-velocity model is not a direct output of the eikonal method. We approximate it calculating the traveltime on a straight ray path between station pairs.

For the real data case, the variance reduction of the purely isotropic model is around 0.8 for short periods up to 25 s (Table 1). At longer periods, it decreases to values close to zero (no improvement compared to the constant velocity model). This behaviour is also observed with classical inversion approaches (Kästle *et al.* 2018) and has three main reasons: (1) the ray approximation used in this test which is not valid for the large wavelengths at longer periods; (2) the data quality decreases above 30 s for the presented ambient-noise measurements making it more difficult to get a good data fit and (3) the phase-velocity model at long periods shows only small velocity variations such that it is always closer to the constant velocity reference model. Including the anisotropy has only a small but positive effect on the variance reduction (∼0.01), improving the data fit which we take as indication that the method is working. We note that, at periods below 30 s, the anisotropic variance reduction gives slightly improved values if we choose to average measurements in within a smaller radius, instead of the 30 km radius applied above.

The variance reduction in the synthetic example in Fig. 6 gives similar values, with a slightly more pronounced effect from including the anisotropy (∼0.03). Of course, there is no period dependence, as the synthetic data are calculated with the same error and same ray approximation for all periods.

5.2 Non-homogeneous noise source distribution and Ψ_4 anisotropy

Ambient-noise based traveltime measurements require a homogeneous distribution of noise sources from all azimuthal directions, otherwise the result may be biased (Yang & Ritzwoller 2008; Tsai 2009; Weaver *et al.* 2009; Yao & van der Hilst 2009; Kästle *et al.* 2016). We have noted earlier that even small errors in the traveltime field can lead locally to large phase-velocity variations and thus an increase in uncertainty of the final phase-velocity maps. An inhomogenous noise-source distribution would likely influence neighboring station measurements similarly and therefore only make a small contribution to the roughness in the traveltime field. Lin *et al.* (2013) similarly argue that the inhomogeneous noise source
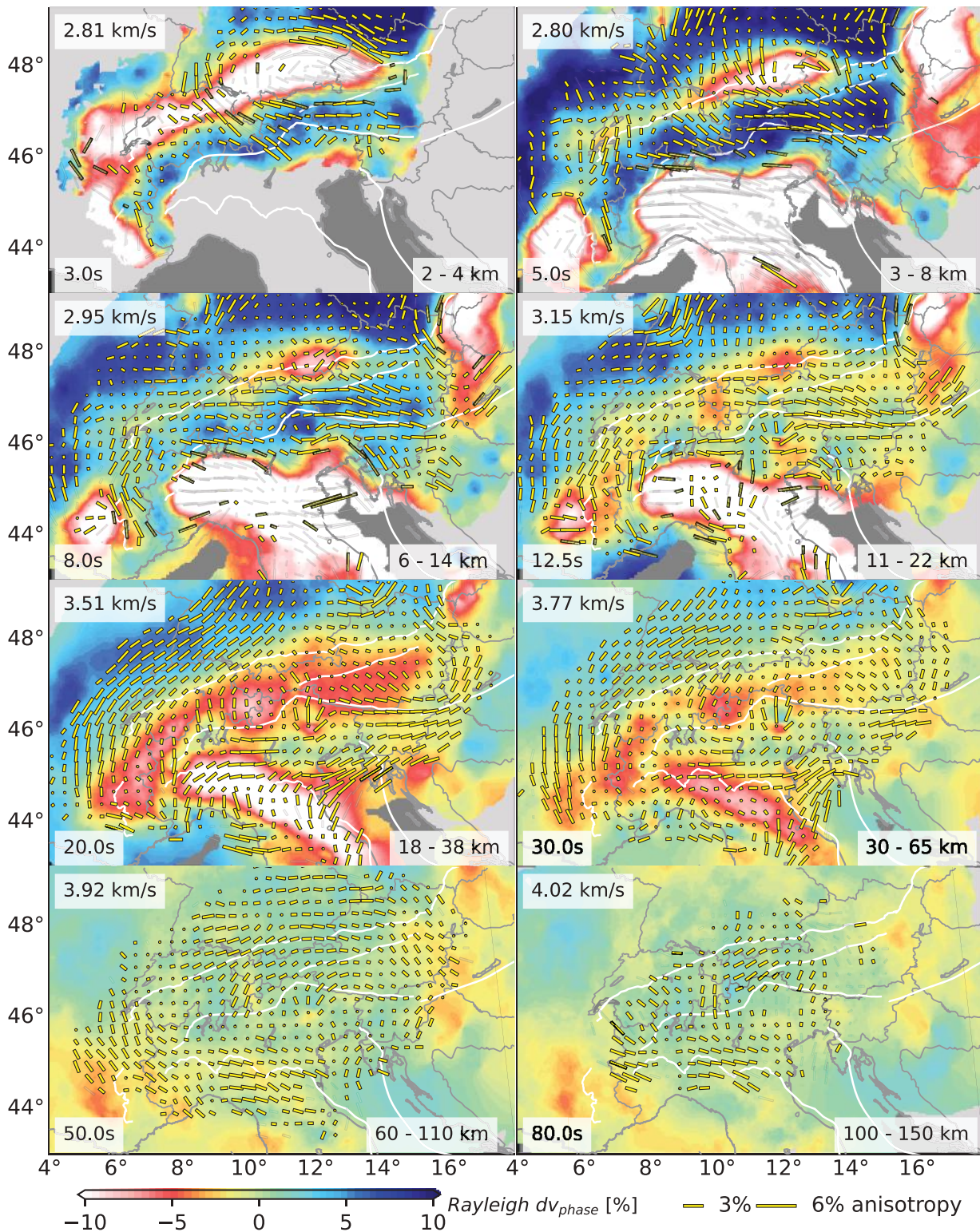
Figure 9. Rayleigh fundamental-mode phase-velocity maps at selected periods. Velocities are given as deviations from the mean velocity shown in the top left corner of each panel. Yellow bars indicate the direction and strength of the azimuthally anisotropic fast axis. Greyed out bars indicate that the standard deviation of A_2 exceeds 0.5. In regions where the majority of the bars are grey the anisotropic parameters are thus likely to be biased. White boundaries show tectonic limits and major faults from Schmid *et al.* (2004).

Table 1. Variance reduction and mean anisotropic amplitudes (percent) at different periods. The variance reduction values are calculated from eq. (4) using the real data results presented in Fig. 9 for the isotropic and anisotropic velocity variations. The variance reduction is always higher when the anisotropy is taken into account except at 50 s period. The anisotropic amplitudes represent an average over the entire mapped area based on the regression applied to eq. (2).

Period	Isotropic	Anisotropic	Avg. A_1	Avg. A_2	Avg. A_4
3.0	0.758	0.793	1.25	1.40	0.96
5.0	0.734	0.764	1.77	1.70	0.90
8.0	0.831	0.843	1.32	1.15	0.72
12.5	0.778	0.791	0.91	0.99	0.56
20.0	0.836	0.856	0.67	0.98	0.37
30.0	0.533	0.558	0.70	0.79	0.44
50.0	0.057	0.052	0.74	0.69	0.54
80.0	0.013	0.021	0.84	0.76	0.76

distribution plays a minor role for the eikonal equation tomography, because the gradients are less influenced, compared to classical straight ray tomography. Also, averaging over the ensemble of phase-velocity maps will cancel out most of this bias. However, for the determination of the anisotropic parameters, the effect may have a negative effect on our final maps. Synthetic tests of Kästle *et al.* (2016) for a typical situation in the Alpine region indicate that the bias from non-homogeneous source distribution varies with a Ψ_4 periodicity with an amplitude of 0.5 per cent. We therefore assume that the bias on the discussed Ψ_2 anisotropy is low compared to the observed anisotropic amplitudes. The observed amplitude of the Ψ_4 anisotropy is always about 30–50 per cent smaller compared to the Ψ_2 anisotropy at periods up to 25 s (Table 1). At longer periods the difference approaches zero. Also in the synthetic example, the amplitudes of the Ψ_4 anisotropy are non-negligible and about 70 per cent smaller than those of the Ψ_2 anisotropy. Our synthetic tests indicate that the spurious Ψ_4 anisotropy is not confined to the region of the anisotropic patches so that we can exclude a mapping of the Ψ_2 anisotropy into the Ψ_4 anisotropy. We can also exclude any bias from a non-homogeneous noise source distribution in the synthetic example. Thus, we infer that part of the Ψ_4 anisotropy is caused by errors in the reconstructed traveltime field, related to data errors and to the sparse sampling of the traveltime field.

5.3 Ψ_1 anisotropy

Tests for the herein presented data set indicate that the Ψ_1 anisotropy appears at all periods and concentrates around certain areas such as the Ivrea zone in the western Alps, the sedimentary basins, and the borders of the mapped region (Fig. 10). The model-averaged amplitude of the Ψ_1 anisotropy is slightly smaller than that of the Ψ_2 anisotropy below 40 s and equal or larger above; the variation is small, however (Table 1). Lin & Ritzwoller (2011b) propose that a strong amplitude of the Ψ_1 anisotropy can be taken as proxy for a bias in Ψ_2. They find in a synthetic test that the spurious Ψ_1 component is strongest at the border of low-velocity zones with their fast-axis pointing towards the fast velocity region. The same is true for the real-data example shown at 8 s period in Fig. 10(a). The synthetic tests of Lin & Ritzwoller (2011b) further show that the spurious Ψ_2 component, tends to be strongest inside the low-velocity regions, aligned with the major elongation axis of the low-velocity patches, similar to Fig. 7(b). We infer that this spurious Ψ_2 component leads to an increase in the A_2 standard deviation. This can be seen from Figs 10(e) and (f) which exhibit both a strong Ψ_1 component but also a larger scatter in the mapped phase velocities,

compared to the points in Figs 10(c) and (d). This justifies our choice of basing our rejection scheme in Fig. 9 on the uncertainty in the amplitude of the Ψ_2 anisotropy which is spatially better correlated with the spurious Ψ_2 component. Different from Lin & Ritzwoller (2011b), we find that the Ψ_1 anisotropy is already pronounced at short periods (Fig. 10 at 8 s period). This may be due to the strong velocity contrasts from the sedimentary basins in our model area which did not play an important role in the studies of Lin & Ritzwoller (2011a, b) that only consider periods ≥40 s. It further indicates that the effect from undersampling of the traveltime field has a similar influence on the mapped anisotropic bias (in Ψ_1, Ψ_2 and Ψ_4) as from finite-frequency effects.

5.4 Sources of anisotropy

Different mechanisms can cause the azimuthal anisotropy in the crust and it is not easy to distinguish between these processes when interpreting the imaged structures. Laboratory experiments on rock samples show that at shallow depth, down to about 200 MPa (∼5 km), the bulk anisotropy is dominated by microcracks (Kern 1990; Kern & Schmidt 1990). These (fluid filled) cracks are expected to be aligned perpendicular to the minimum stress direction and thus approximately parallel to the maximum horizontal stress and the anisotropic fast axis (Crampin 1994). An alignment of the fast axis is also expected with structures such as rock foliation (Lüschen *et al.* 1991), faults, folds or inclusions. All of these effects can be summarized as shape-preferred orientation (SPO) of the anisotropic fast axis. In contrast, the alignment of anisotropic crystals such as olivine (e.g. Nicolas & Christensen 1987), mainly in the mantle, or amphibole and biotite (Barruol & Mainprice 1993) which are also abundant in the lower crust, is classified as lattice-preferred orientation (LPO) and is the main source of anisotropy at greater depths. The named minerals show an alignment of their fast axis parallel to the main strain direction, however, other minerals such as pyroxene can have an opposite effect (fast axis perpendicular to the strain direction) and thus lower the observed bulk anisotropy (Barruol & Mainprice 1993; Silver 1996). In this work, we will apply the simplified assumption that the bulk LPO, and thus the anisotropic fast axis, is aligned parallel to the main strain direction.

5.5 Tectonic interpretation of the anisotropy pattern

The methodological uncertainties described above demand caution when interpreting the Ψ_2 anisotropic pattern. We will thus focus on areas where the potential bias is low (yellow bars in Fig. 9). Our results indicate that in the valid model regions, the entire crust and uppermost mantle is affected by moderate levels (1–4 per cent) of azimuthal anisotropy. This is different from recent results of the radially anisotropic structure which show anisotropy mostly underneath the Alpine and the Apenninic orogens (Alder *et al.* 2021). A comparison between our results and this study is difficult because of methodological differences and the different sensitivities of azimuthal and radial anisotropy to vertically/horizontally aligned fast axis.

The average principal stress direction in the Alps is N–S oriented except for the northern part of the western Alps and transition from eastern Alps to the Pannonian basin where an E–W orientation dominates (Fig. 1). According to the discussion above, we expect a parallel alignment of the fast axis direction with the principal stress direction at shallow depth. The shortest-period anisotropic measurements (3–5 s) have large uncertainties due to a stronger bias that make a conclusive comparison with the stress direction
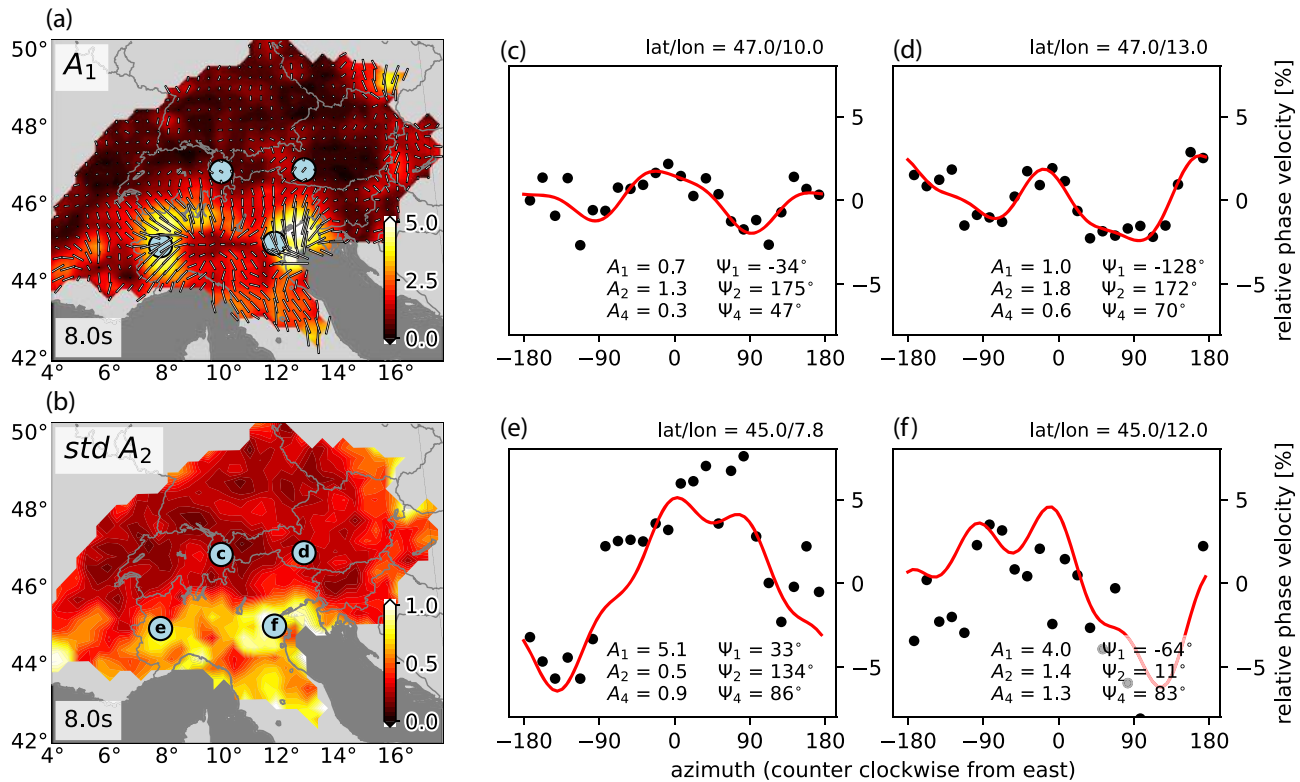
Figure 10. Azimuthal anisotropy at selected locations for the phase-velocity map at 8 s period. (a) Amplitude of the Ψ_1 anisotropy and its direction. (b): Standard deviation of A_2. (c)–(f) Mean velocities obtained in different azimuthal directions (black dots) and the regression fit (red line). The anisotropic parameters shown at the bottom of each panel correspond to those in eq. (2). The data for the panels (c)–(f) were taken from circular regions with 30 km radius as indicated in panels (a) and (b).

difficult. An agreement between principal stress direction and fast axis orientation is only visible in few parts of the map such as in parts of the central Alps and at the eastern edge of the eastern Alps. This may be due to the discussed methodological uncertainties, but the anisotropy may also be dominated by fault and fold structures instead of the stress field. In the eastern Alps, we infer from the higher phase velocities that the depth sensitivity of the Rayleigh waves should be deeper (Fig. S1) and thus the peak sensitivity may already lie below the 5 km estimate for the stress dominated anisotropic fast-axis alignment. A stress-related fast axis orientation at short periods is also proposed by Schippkus *et al.* (2018, 2019) who study the anisotropy in the Vienna basin region (Fig. S12). A direct comparison between the studies is not possible, because Schippkus *et al.* (2019) use group velocities that have a different depth sensitivity; the strong velocity contrast to the adjacent low-velocity basin and the position at the edge of our model area limits the interpretability of the results in our study. The observed anisotropic fast axis curve around the low-velocity Vienna basin and are aligned in SW–NE direction within the basin correspond very well to the bias modeled in Fig. 7 and are accordingly greyed out in Fig. 9.

For the mid-to lower crustal depths, we can compare our results to the study of Fry *et al.* (2010) who image the azimuthal anisotropy in Switzerland at periods between 8 and 40 s (Fig. 11). Both the isotropic and the anisotropic part are highly compatible between the two models up to a period of 24 s. In this period range, the fast axis are aligned roughly parallel to the arcuation of the Alpine orogen. Also in the western and northwestern foreland, this orientation can be observed (Fig. 9). This may be due to major thrust

faults that formed the Alpine edifice but also other major lineaments such as the Periadiatic line (Fig. 1). Alternatively, LPO of crustal minerals due to compression (Fry *et al.* 2010) could cause this pattern. From 8 to 24 s period (transition from mid to lower crust in the Alps), a change in fast axis orientation from arc-parallel to arc-perpendicular can be observed (Fry *et al.* 2010). The northern limit of the arc-perpendicular orientation at 16 and 24 s coincides spatially with the Alpine front. It is interpreted by Fry *et al.* (2010) in terms of lower European crust which is uplifting in slices after European slab break-off and following slab retreat. In their model, this results in two displacement components, a vertical one, which is not imaged by the azimuthal anisotropy, and a northward one, which gives the arc-perpendicular orientation. This mechanism has been thermomechanically modeled showing both a northward and vertical component of the lower crustal stress tensor (Singer *et al.* 2014). According to our results, this process would be limited to the central Alps, as we do not observe a clear arc-perpendicular fast-axis orientation in the eastern or western Alps at periods between 20 and 30 s. This would be in agreement with models that suggest an attached slab in the central, but detached subduction slabs in the western and eastern Alps (Kästle *et al.* 2020; Paffrath *et al.* 2021; Handy *et al.* 2021).

In the eastern Alps, we expect to see an imprint of the eastward extrusion (Frisch *et al.* 1998) in the anisotropic fast-axis directions. Indeed, we observe higher, E-W oriented, anisotropic amplitudes between 3 and 20 s, compared to the rest of the Alps. The SEMP fault to the north, and the Periadriatic line to the south (Fig. 1) limit the extrusion area in agreement with the highest observed Ψ_2 amplitudes at 8 and 12.5 s. We infer that the E–W pattern may be
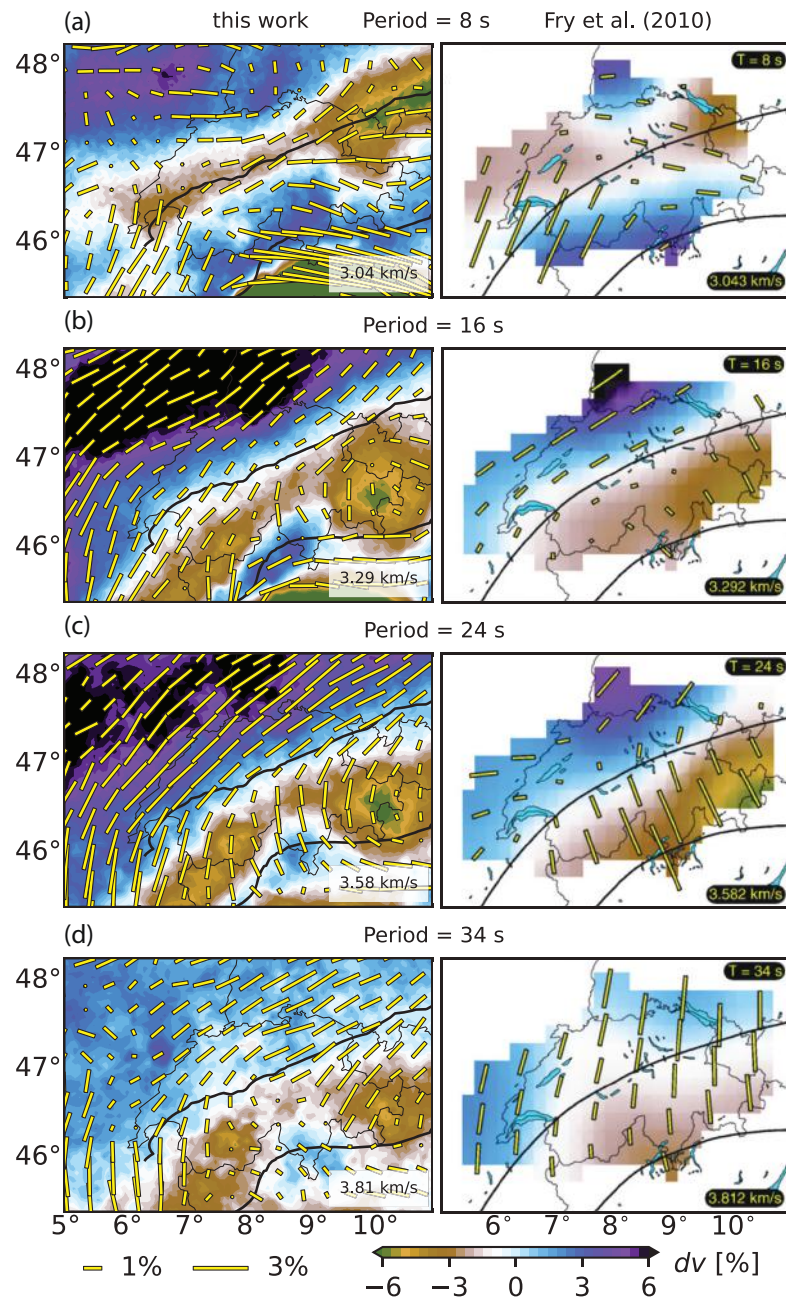
Figure 11. Comparison of the isotropic and anisotropic phase-velocity maps in Switzerland between this work (left-hand panels) and the one of Fry *et al.* (2010, right-hand panels) at four different periods (a) 8 s, (b) 16 s, (c) 24 s and (d) 34 s. The colour model and the length of the anisotropic bars have been adapted to provide comparability between the models.

due to LPO of the minerals, parallel to the eastward motion. Above 12.5 s period, the E–W orientation is most prominent around the Periadriatic Fault zone which thus seems to affect the structure down to the lowermost crustal depths.

The measured Rayleigh waves start sampling the uppermost, lithospheric mantle above periods of about 20 s in the forelands, and 40 s in the Alps (sensitivity kernels in Fig. S1). This is largely controlled by the crustal thickness variations as can be seen from the lower velocities underneath the Alps, for example at 20 s period. Fry *et al.* (2010) find that at these periods, the fast axis in Switzerland orient consistently in N–S direction. We do not observe the same pattern, instead the images in Fig. 11 suggest a continuation of

the arc-parallel anisotropic fast axis orientation in the western and northern Alpine foreland up to approximately 50 s. The arc-parallel foreland structure can be followed eastwards to about 13°E where they turn northwards. This coincides spatially with the border to the Bohemian Massif (Fig. 1). We infer thus that there may be LPO orientation in the uppermost, lithospheric mantle in the European plate. The herein presented results are compared to those obtained with Pn waves (sensitive to the uppermost mantle; Diaz *et al.* 2013) and a compilation of SKS results (most sensitive to the upper mantle; Wüstefeld *et al.* 2009,and references therein) in Fig. 12. At 20 s period, the fast axis orientations in the northern Alpine foreland are highly compatible between Pn- and surface-wave results, including
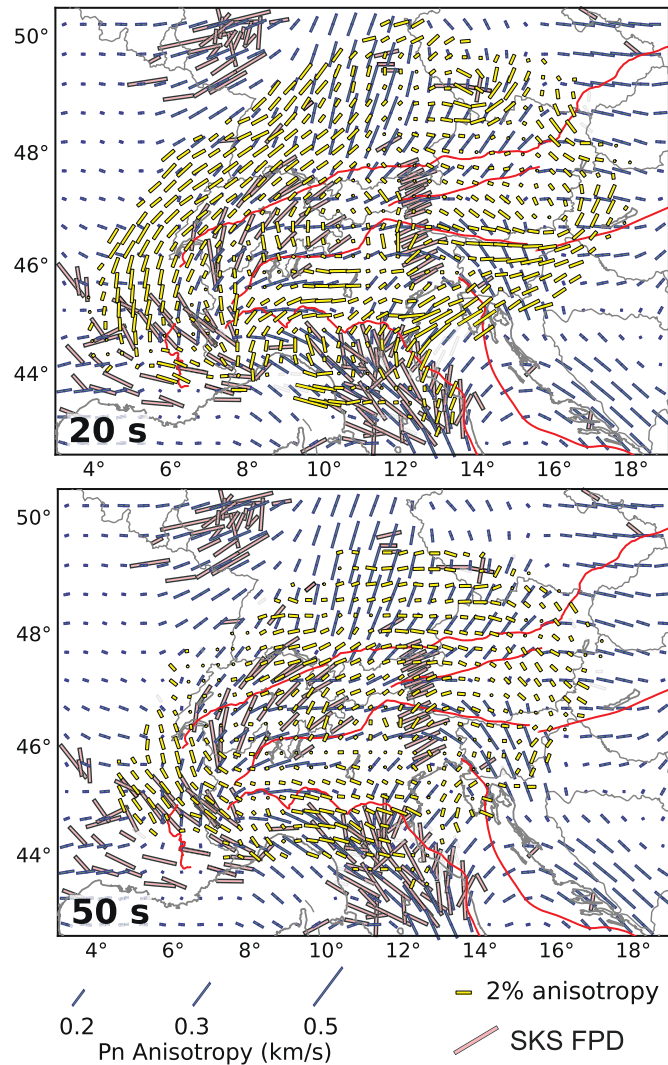
Figure 12. Comparison between Pn anisotropy from Diaz *et al.* (2013, blue bars), a compilation of SKS fast propagation directions (SKS FPD, light red bars) modified from Wüstefeld *et al.* (2009); Diaz *et al.* (2013) and the anisotropic fast-axis results from this work (yellow bars) at 20 and 50 s period. The red lines indicate major tectonic lineaments (Fig. 1).

the arc-parallel flow that turns northward at approx. 10°E. Within the Alps, the 20 s surface waves are mostly sampling the lowermost crustal structure and therefore Pn results and those from this work do not match well. SKS waves are sensitive to deeper structure and thus we see the best compatibility for long periods surface waves (Fig. 12). Both methods show the well known flow field around the western Alps and the arc-parallel orientation under the Alps and underneath both southern and northern forelands (Wüstefeld *et al.* 2009; Barruol *et al.* 2011; Salimbeni *et al.* 2018; Petrescu *et al.* 2020). The herein presented surface-wave results thus help to better understand the depth-sensitivity of SKS splitting studies in the Alpine region.

6   CONCLUSIONS

We extract phase-dispersion curves from ambient-noise cross correlations for 2 yr of AlpArray data. The resulting Rayleigh-wave phase-velocity measurements are used to obtain azimuthally anisotropic maps at periods between 3 and 80 s with the eikonal tomography method.

Through a suite of synthetic tests, we illustrate how strong velocity variations may bias the mapped anisotropy. We attribute the bias to two mechanisms: (1) finite frequency effects that directly affect the phase velocity measurements between station pairs. These are caused by low-velocity zones that can produce a secondary wave front downstream from the velocity anomaly and interference between direct and reflected/refracted and/or multiple waves. These produced artefacts are period-dependent and can be significantly reduced if the amplitude information is taken into account (Helmholtz tomography). This is, however, only possible if good amplitude information at densely spaced sample (i.e. station) locations is available. (2) Artefacts due to incomplete sampling of the traveltime field. This problem is most pronounced at short periods where the wave front is very complex and thus only a smoothed and distorted traveltime field can be recovered. We show that at short periods (relative to the interstation spacing and the strength of the wave-field distortion due to velocity heterogeneities), the undersampling is responsible for most of the reported bias.

The spurious Ψ_2 anisotropy appears most prominent within low-velocity regions and at the borders of large velocity contrasts. For the shown application to the AlpArray network with typical station

spacing of 50 km, a bias from velocity heterogeneities of ± 10 per cent and less seems negligible, at the herein studied periods. In the isotropic velocity distribution, most of the bias cancels out, given that there is good azimuthal coverage.

We find that the anisotropic bias has a rough spatial correlation with the amplitude of the Ψ_1 anisotropy and the mapped uncertainty in A_2, with the latter being more consistent. We therefore use the A_2 uncertainty as indicator for potentially biased regions in our final maps and we exclude anisotropy estimates for those regions from our final maps. For the remaining regions in the real data maps we interpret the anisotropic structures as follows:

(i) At mid-crustal depths, an E–W orientation of the anisotropic fast axis is observed in the entire Alpine arc. This could be explained with the orientation of major faults and lineaments and the LPO of crystals due to compression as proposed by Fry *et al.* (2010).

(ii) In the lower crust, an arc-perpendicular pattern emerges in the central Alps. In the eastern Alps, the pattern remains rather E–W oriented. We interpret the consistent E–W orientation in the eastern Alps as imprint of the eastward extrusion and find the most pronounced effect on the anisotropic fast axis around the eastern Periadriatic Fault zone.

(iii) In the northern Alpine foreland a simple, arc-parallel pattern of fast axis becomes visible at lower crustal and uppermost mantle depths, limited in the east by the Bohemian Massif. This orientation is similar to the one observed from Pn waves and in SKS studies and is probably related to the Alpine orogeny.

DATA AVAILABILITY

The data from the AlpArray experiment is distributed through OR-FEUS and EIDA (www.orfeus-eu.org/data/eida/) and freely accessible to all AlpArray Working Group members (www.alparray.ethz.ch/en/organisation/partecipants/). The data will become publicly accessible by March 2022. The AlpArray Seismic Network comprises the temporary AlpArray stations (Z3 2015) and the following permanent networks: BW (2001); CH (1983); CR (2001); CZ (1973); FR (1995); HU (1992); G (1982); GE (1993); GR (1976); GU (1967); HS (2012); IU (1988); NI (2002); OE (1987); OX (2016); RD (2018); RF (1993); SK (2004); SL (1990); ST (1981); SX (2001); TH (2009).

REFERENCES

Aki, K., 1957. Space and time spectra of stationary stochastic waves, with special reference to microtremors, *Bull. Earthq. Res. Inst., Univ. Tokyo,* **35**(3), 415–456.

Albuquerque Seismological Laboratory (ASL)/USGS. (1988). *Global Seismograph Network - IRIS/USGS [Data set]*. International Federation of Digital Seismograph Networks. https://doi.org/10.7914/SN/IU.

Alder, C., Debayle, E., Bodin, T., Paul, A., Stehly, L., Pedersen, H., *et al.*, 2021. Evidence for radial anisotropy in the lower crust of the Apennines from Bayesian ambient noise tomography in Europe, *J. geophys. Int.,* **226**(2), 941–967.

AlpArray Seismic Network. (2015). *AlpArray Seismic Network (AASN) temporary component*. AlpArray Working group. https://doi.org/10.12686/alparray/z3_2015.

Barruol, G. & Mainprice, D., 1993. 3-D seismic velocities calculated from lattice-preferred orientation and reflectivity of a lower crustal section: examples of the Val Sesia section (Ivrea zone northern Italy), *J. geophys. Int.,* **115**(3), 1169–1188.

Barruol, G., Bonnin, M., Pedersen, H., Bokelmann, G.H. & Tiberi, C., 2011. Belt-parallel mantle flow beneath a halted continental collision: The Western Alps, *Earth planet. Sci. Lett.,* **302**(3–4), 429–438.

Bennett, L., Melchers, B. & Proppe, B., 2020. Curta: a general-purpose high-performance computer at ZEDAT, Freie Universität Berlin, Tech. rep., Freie Universität Berlin.

Beyreuther, M., Barsch, R., Krischer, L., Megies, T., Behr, Y. & Wassermann, J., 2010. ObsPy: a Python Toolbox for seismology, *Seismol. Res. Lett.,* **81**(3), 530–533.

Bodin, T. & Maupin, V., 2008. Resolution potential of surface wave phase velocity measurements at small arrays, *J. geophys. Int.,* **172**(2), 698–706.

Boschi, L. & Dziewonski, A.M., 1999. High- and low-resolution images of the Earth's mantle: Implications of different approaches to tomographic modeling, *J. geophys. Res.,* **104**(B11), 25 567–25 594.

Boue, P., Poli, P., Campillo, M., Pedersen, H., Briand, X. & Roux, P., 2013. Teleseismic correlations of ambient seismic noise for deep global imaging of the Earth, *J. geophys. Int.,* **194**(2), 844–848.

Carminati, E., Lustrino, M. & Doglioni, C., 2012. Geodynamic evolution of the central and western Mediterranean: Tectonics vs. igneous petrology constraints, *Tectonophysics,* **579**, 173–192.

Charles University in Prague (Czech), Institute of Geonics, Institute of Geophysics, Academy of Sciences of the Czech Republic, Institute of Physics of the Earth Masaryk University (Czech), & Institute of Rock Structure and Mechanics. (1973). *Czech Regional Seismic Network [Data set]*. International Federation of Digital Seismograph Networks. https://doi.org/10.7914/SN/CZ.

Crampin, S., 1994. The fracture criticality of crustal rocks, *J. geophys. Int.,* **118**(2), 428–438.

Department of Earth and Environmental Sciences, Geophysical Observatory, University of Munchen. (2001). *BayernNetz [Data set]*. International Federation of Digital Seismograph Networks. https://doi.org/10.7914/SN/BW.

de Ridder, S. & Dellinger, J., 2011. Ambient seismic noise eikonal tomography for near-surface imaging at Valhall, *Leading Edge,* **30**(5), 506–512.

Diaz, J., Gil, A. & Gallart, J., 2013. Uppermost mantle seismic velocity and anisotropy in the Euro-Mediterranean region from pn and sn tomography, *J. geophys. Int.,* **192**(1), 310–325.

Dziewonski, A.M., Chou, T.-A. & Woodhouse, J.H., 1981. Determination of earthquake source parameters from waveform data for studies of global and regional seismicity, *J. geophys. Res.,* **86**(B4), 2825–2852.

Ekström, G., 2001. Time domain analysis of Earth's long-period background seismic radiation, *J. geophys. Res.,* **106**(B11), 26483–26493.

Ekström, G., Abers, G.A. & Webb, S.C., 2009. Determination of surface-wave phase velocities across USArray from noise and Aki's spectral formulation, *Geophys. Res. Lett.,* **36**(18), doi:10.1029/2009gl039131.

Ekström, G., Nettles, M. & Dziewoński, A., 2012. The global CMT project 2004–2010: centroid-moment tensors for 13,017 earthquakes, *Phys. Earth planet. Inter.,* **200-201,** 1–9.

ESI SAS (Earth Science Institute Of The Slovak Academy Of Sciences). (2004). *National Network of Seismic Stations of Slovakia. Deutsches GeoForschungsZentrum GFZ.* https://doi.org/10.14470/FX099882.

Federal Institute for Geosciences and Natural Resources. (1976). *German Regional Seismic Network (GRSN).* Bundesanstalt für Geowissenschaften und Rohstoffe. https://doi.org/10.25928/mbx6-hr74.

Feng, L. & Ritzwoller, M.H., 2017. The effect of sedimentary basins on surface waves that pass through them, *J. geophys. Int.,* **211**(1), 572–592.

Fichtner, A., Bowden, D. & Ermert, L., 2020. Optimal processing for seismic noise correlations, *J. geophys. Int.,* **223**(3), 1548–1564.

Franke, W., Cocks, L.R.M. & Torsvik, T.H., 2017. The palaeozoic variscan oceans revisited, *Gondwana Res.,* **48,** 257–284.

Friederich, W., Hunzinger, S. & Wielandt, E., 2000. A note on the interpretation of seismic surface waves over three - dimensional structures, *J. geophys. Int.,* **143**(2), 335–339.

Frisch, W., Kuhlemann, J., Dunkl, I. & Brügel, A., 1998. Palinspastic reconstruction and topographic evolution of the Eastern Alps during late Tertiary tectonic extrusion, *Tectonophysics,* **297**(1–4), 1–15.

Fry, B., Deschamps, F., Kissling, E., Stehly, L. & Giardini, D., 2010. Layered azimuthal anisotropy of Rayleigh wave phase velocities in the European Alpine lithosphere inferred from ambient noise, *Earth planet. Sci. Lett.,* **297**(1–2), 95–102.

Gallego, A., Panning, M., Russo, R., Comte, D., Mocanu, V., Murdie, R. & Vandecar, J., 2011. Azimuthal anisotropy in the Chile Ridge subduction region retrieved from ambient noise, *Lithosphere,* **3**(6), 393–400.

GEOFON Data Centre. (1993). *GEOFON Seismic Network.* Deutsches GeoForschungsZentrum GFZ. https://doi.org/10.14470/TR560404.

Geological Survey-Provincia Autonoma di Trento. (1981). *Trentino Seismic Network [Data set].* International Federation of Digital Seismograph Networks. https://doi.org/10.7914/SN/ST.

Guo, Z., Gao, X., Yao, H. & Wang, W., 2017. Depth variations of azimuthal anisotropy beneath the Tian Shan Mt range (NW China) from ambient noise tomography, *J. Asian Earth Sci.,* **138,** 161–172.

Handy, M., Schmid, S., Paffrath, M., Friederich, W., Group, A.W., *et al.*, 2021. European tectosphere and slabs beneath the greater alpine area– interpretation of mantle structure in the Alps-Apennines-Pannonian region from teleseismic Vp studies, *Solid Earth Discuss.,* [preprint], https://doi.org/10.5194/se-2021-49, in review, 1–61.

Handy, M.R., Schmid, S.M., Bousquet, R., Kissling, E. & Bernoulli, D., 2010. Reconciling plate-tectonic reconstructions of Alpine Tethys with the geological–geophysical record of spreading and subduction in the Alps, *Earth-Sci. Rev.,* **102**(3–4), 121–158.

Handy, M.R., Ustaszewski, K. & Kissling, E., 2014. Reconstructing the Alps–Carpathians–Dinarides as a key to understanding switches in subduction polarity slab gaps and surface motion, *Int. J. Earth Sci.,* **104**(1), 1–26.

Heidbach, O., Rajabi, M., Reiter, K., Ziegler, M. & Team, W., 2016. World stress map database release 2016 V. 1.1, doi.10.5880/WSM.2016.001.

Hetényi, G., *et al.*, 2018. The AlpArray seismic network: a large-scale european experiment to image the Alpine Orogen, *Surv. Geophys.,* **39**(5), 1009–1033.

Hessian Agency for Nature Conservation, Environment and Geology. (2012). *Hessischer Erdbebendienst [Data set].* International Federation of Digital Seismograph Networks. https://doi.org/10.7914/SN/HS.

Institut De Physique Du Globe De Paris (IPGP) , & Ecole Et Observatoire Des Sciences De La Terre De Strasbourg (EOST). (1982). *GEOSCOPE, French Global Network of broad band seismic stations.* Institut de physique du globe de Paris (IPGP), Université de Paris. https://doi.org/10.18715/GEOSCOPE.G.

Institut fuer Geowissenschaften, Friedrich-Schiller-Universitaet Jena. (2009). *Thüringer Seismologisches Netz [Data set].* International Federation of Digital Seismograph Networks. https://doi.org/10.7914/SN/TH.

Istituto Nazionale di Oceanografia e di Geofisica Sperimentale - OGS. (2016). *North-East Italy Seismic Network [Data set].* Tech. rep., OGS (Istituto Nazionale Di Oceanografia E Di Geofisica Sperimentale). FDSN. https://doi.org/10.7914/SN/OX.

Köveslighety Radó Seismological Observatory (Geodetic And Geophysical Institute, Research Centre For Astronomy And Earth Sciences, Hungarian Academy Of Sciences (MTA CSFK GGI KRSZO)). (1992). *Hungarian National Seismological Network.* Deutsches GeoForschungsZentrum GFZ. https://doi.org/10.14470/UH028726.

Kern, H., 1990. Laboratory seismic measurements: an aid in the interpretation of seismic field data, *Terra Nova,* **2**(6), 617–628.

Kern, H. & Schmidt, R., 1990. Physical properties of KTB core samples at simulated in situ conditions, *Scient. Drilling,* **1**(5), 217–223.

Kissling, E. & Schlunegger, F., 2018. Rollback Orogeny model for the evolution of the Swiss Alps, *Tectonics,* **37**(4), 1097–1115.

Kästle, E.D., Soomro, R., Weemstra, C., Boschi, L. & Meier, T., 2016. Two-receiver measurements of phase velocity: cross-validation of ambient-noise and earthquake-based observations, *J. geophys. Int.,* **207**(3), 1493–1512.

Kästle, E.D., El-Sharkawy, A., Boschi, L., Meier, T., Rosenberg, C., Bellahsen, N., Cristiano, L. & Weidle, C., 2018. Surface wave tomography of the Alps using ambient-noise and earthquake phase velocity measurements, *J. geophys. Res.,* **123**(2), 1770–1792.

Kästle, E.D., Rosenberg, C., Boschi, L., Bellahsen, N., Meier, T. & El-Sharkawy, A., 2020. Slab break-offs in the Alpine subduction zone, *Int. J. Earth Sci.,* **109**(2), 587–603.

Lehujeur, M. & Chevrot, S., 2020. On the validity of the eikonal equation for surface-wave phase-velocity tomography, *J. geophys. Int.,* **223**(2), 908–914.

Lin, F.-C. & Ritzwoller, M.H., 2011a. Helmholtz surface wave tomography for isotropic and azimuthally anisotropic structure, *J. geophys. Int.,* **186**(3), 1104–1120.

Lin, F.-C. & Ritzwoller, M.H., 2011b. Apparent anisotropy in inhomogeneous isotropic media, *J. geophys. Int.,* **186**(3), 1205–1219.

Lin, F.-C., Ritzwoller, M.H. & Snieder, R., 2009. Eikonal tomography: surface wave tomography by phase front tracking across a regional broadband seismic array, *J. geophys. Int.,* **177**(3), 1091–1110.

Lin, F.-C., Li, D., Clayton, R.W. & Hollis, D., 2013. High-resolution 3D shallow crustal structure in Long Beach California: application of ambient noise tomography on a dense seismic array, *Geophysics,* **78**(4), Q45–Q56.

Louboutin, M., Lange, M., Luporini, F., Kukreja, N., Witte, P.A., Herrmann, F.J., Velesko, P. & Gorman, G.J., 2019. Devito (v3.1.0): an embedded domain-specific language for finite differences and geophysical exploration, *Geoscient. Model Dev.,* **12**(3), 1165–1187.

Lüschen, E., Söllner, W., Hohrath, A. & Rabbel, W., 1991. Integrated P- and S-wave borehole experiments at the KTB-deep drilling site in the Oberpfalz area (SE Germany), in *Continental Lithosphere: Deep Seismic Reflections,* Vol. **22,** pp. 121–133, Meissner, R.,Brown, L., Dürbaum, H.-J., Franke, W., Fuchs, K. & Seifert, F., American Geophysical Union.

Lu, Y., 2019. *Tomography of the Alpine Arc Using Noise Correlations Waveform Modelling, PhD thesis,* Université Grenoble Alpes.

Lu, Y., Stehly, L. & and, A.P., 2018. High-resolution surface wave tomography of the European crust and uppermost mantle from ambient seismic noise, *J. geophys. Int.,* **214**(2), 1136–1150.

Luporini, F., *et al.*, 2018. Architecture and performance of Devito, a system for automated stencil computation, *ACM Trans. Math. Softw.,* **46**(1), 1–28, doi:10.1145/3374916.

Malusà, M.G., *et al.*, 2015. Contrasting styles of (U) HP rock exhumation along the Cenozoic Adria-Europe plate boundary (Western Alps, Calabria, Corsica), *Geochem. Geophys. Geosyst.,* **16**(6), 1786–1824.

Mordret, A., Shapiro, N.M., Singh, S.S., Roux, P. & Barkved, O.I., 2013. Helmholtz tomography of ambient noise surface wave data to estimate Scholte wave phase velocity at Valhall Life of the Field, *Geophysics,* **78**(2), WA99–WA109.

Nicolas, A. & Christensen, N.I., 1987. Formation of anisotropy in upper mantle peridotites: a review, in *Composition Structure and Dynamics of the Lithosphere-Asthenosphere System,* pp. 111–123, eds Fuchs, K. & Froidevaux, C., American Geophysical Union.

Nolet, G. & Dahlen, F.A., 2000. Wave front healing and the evolution of seismic delay times, *J. geophys. Res.,* **105**(B8), 19 043–19 054.

OGS (Istituto Nazionale di Oceanografia e di Geofisica Sperimentale) and University of Trieste. (2002). *North-East Italy Broadband Network [Data set]*. International Federation of Digital Seismograph Networks. https://doi.org/10.7914/SN/NI.

Paffrath, M., Friederich, W., AlpArray, working group, A.-S.D., *et al.*, 2021. Imaging structure and geometry of slabs in the greater alpine area–a p-wave traveltime tomography using AlpArray seismic network data, *Solid Earth Discuss.,* 1–40.

Petrescu, L., Pondrelli, S., Salimbeni, S., Faccenda, M., Group, A.W., *et al.*, 2020. Mantle flow below the central and greater alpine region: insights from sks anisotropy analysis at AlpArray and permanent stations, *Solid Earth,* **11**(4), 1275–1290.

Qorbani, E., Bianchi, I. & Bokelmann, G., 2015. Slab detachment under the Eastern Alps seen by seismic anisotropy, *Earth planet. Sci. Lett.,* **409**, 96–108.

RESIF. (1995). *RESIF-RLBP French Broad-band network, RESIF-RAP strong motion network and other seismic stations in metropolitan France [Data set]*. RESIF - Réseau Sismologique et géodésique Français. https://doi.org/10.15778/RESIF.FR.

RESIF. (2018). *CEA/DASE broad-band permanent network in metropolitan France [Data set]*. RESIF - Réseau Sismologique et géodésique Français. https://doi.org/10.15778/RESIF.RD.

Salimbeni, S., *et al.*, 2018. Active and fossil mantle flows in the western alpine region unravelled by seismic anisotropy analysis and high-resolution p wave tomography, *Tectonophysics,* **731**, 35–47.

Scharf, A., Handy, M., Favaro, S., Schmid, S.M. & Bertrand, A., 2013. Modes of orogen-parallel stretching and extensional exhumation in response to microplate indentation and roll-back subduction (Tauern Window, Eastern Alps), *Int. J. Earth Sci.,* **102**(6), 1627–1654.

Schippkus, S., Zigone, D., Bokelmann, G. & the AlpArray Working, Group, 2018. Ambient-noise tomography of the wider Vienna Basin region, *J. geophys. Int.,* **215**(1), 102–117.

Schippkus, S., *et al.*, 2019. Azimuthal anisotropy in the wider Vienna basin region: a proxy for the present-day stress field and deformation, *J. geophys. Int.,* **220**(3), 2056–2067.

Schmid, S.M., Fügenschuh, B., Kissling, E. & Schuster, R., 2004. Tectonic map and overall architecture of the Alpine orogen, *Eclogae Geol. Helvet.,* **97**(1), 93–117.

Schmid, S.M., Bernoulli, D., Fügenschuh, B., Matenco, L., Schefer, S., Schuster, R., Tischler, M. & Ustaszewski, K., 2008. The Alpine-Carpathian-Dinaridic orogenic system: correlation and evolution of tectonic units, *Swiss J. Geosci.,* **101**(1), 139–183.

Schulmann, K. & Gayer, R., 2000. A model for a continental accretionary wedge developed by oblique collision: the NE Bohemian Massif, *J. Geol. Soc.,* **157**(2), 401–416.

Shearer, P.M., 2009. *Introduction to Seismology,* Cambridge Univ. Press.

Silver, P.G., 1996. Seismic anisotropy beneath the continents: probing the depths of geology, *Ann. Rev. Earth planet. Sci.,* **24**(1), 385–432.

Singer, J., Diehl, T., Husen, S., Kissling, E. & Duretz, T., 2014. Alpine lithosphere slab rollback causing lower crustal seismicity in northern foreland, *Earth planet. Sci. Lett.,* **397**, 42–56.

Slovenian Environment Agency. (1990). *Seismic Network of the Republic of Slovenia [Data set]*. International Federation of Digital Seismograph Networks. https://doi.org/10.7914/SN/SL.

Smith, M.L. & Dahlen, F.A., 1973. The azimuthal dependence of Love and Rayleigh wave propagation in a slightly anisotropic medium, *J. geophys. Res.,* **78**(17), 3321–3333.

Smith, W.H.F. & Wessel, P., 1990. Gridding with continuous curvature splines in tension, *Geophysics,* **55**(3), 293–305.

Swiss Seismological Service (SED) At ETH Zurich. (1983). *National Seismic Networks of Switzerland*. ETH Zürich. https://doi.org/10.12686/sed/networks/ch.

Tsai, V.C., 2009. On establishing the accuracy of noise tomography travel-time measurements in a realistic medium, *J. geophys. Int.,* **178**(3), 1555–1564.

University of Genoa. (1967). *Regional Seismic Network of North Western Italy [Data set]*. International Federation of Digital Seismograph Networks. https://doi.org/10.7914/SN/GU.

University of Leipzig. (2001). *SXNET Saxon Seismic Network [Data set]*. International Federation of Digital Seismograph Networks. https://doi.org/10.7914/SN/SX.

University of Trieste. (1993). *Friuli Venezia Giulia Accelerometric Network [Data set]*. International Federation of Digital Seismograph Networks. https://doi.org/10.7914/SN/RF.

University of Zagreb. (2001). *Croatian Seismograph Network [Data set]*. International Federation of Digital Seismograph Networks. https://doi.org/10.7914/SN/CR.

Verwater, V.F., Le Breton, E., Handy, M.R., Picotti, V., Jozi Najafabadi, A. & Haberland, C., 2021. Neogene kinematics of the Giudicarie belt and eastern southern alpine orogenic front (Northern Italy), *Solid Earth,* **12**(6), 1309–1334.

Weaver, R., Froment, B. & Campillo, M., 2009. On the correlation of non-isotropically distributed ballistic scalar diffuse waves, *J. acoust. Soc. Am.,* **126**(4), 1817.

Wielandt, E., 1993. Propagation and structural interpretation of non-plane waves, *J. geophys. Int.,* **113**(1), 45–53.

Wüsteleld, A., Bokelmann, G., Barruol, G. & Montagner, J.-P., 2009. Identifying global seismic anisotropy patterns by correlating shear-wave splitting and surface-wave data, *Phys. Earth planet. Inter.,* **176**(3–4), 198–212.

Xu, H., Luo, Y., Chen, C. & Xu, Y., 2016. 3D shallow structures in the Baogutu area Karamay, determined by eikonal tomography of short-period ambient noise surface waves, *J. appl. Geophys.,* **129**, 101–110.

Yang, Y. & Ritzwoller, M.H., 2008. Characteristics of ambient seismic noise as a source for surface wave tomography, *Geochem. Geophys., Geosyst.,* **9**(2), doi:10.1029/2007GC001814.

Yao, H. & van der Hilst, R.D., 2009. Analysis of ambient noise energy distribution and phase velocity bias in ambient noise tomography with application to SE Tibet, *J. geophys. Int.,* **179**(2), 1113–1132.

ZAMG - Zentralanstalt für Meterologie und Geodynamik. (1987). *Austrian Seismic Network [Data set]*. International Federation of Digital Seismograph Networks. https://doi.org/10.7914/SN/OE.

Zhao, L., *et al.*, 2015. First seismic evidence for continental subduction beneath the western alps, *Geology,* **43**(9), 815–818.

SUPPORTING INFORMATION

Supplementary data are available at *GJI* online.

Figure S1: Rayleigh fundamental mode phase sensitivity kernels for three different shear-velocity profiles, representative of different map regions. The period for each kernel is indicated next to black dot which marks the sensitivity peak. The kernel amplitude indicates which depth levels are sampled by a Rayleigh wave of certain period. The shape of the kernel is strongly influenced by the location of the velocity jumps between sedimentary cover and underlying crustal rocks, as well as between crust and mantle. The shear-velocity profiles are extracted from the model of (Kästle *et al.* 2018).

Figure S2: Comparison of different traveltime interpolation methods. The results are very similar between linear radial basis function (RBF) interpolation, spline-in-tension interpolation (Smith & Wessel 1990), linear and cubic interpolation. Linear interpolation results in a more blocky model. Cubic interpolation can yield very high spurious amplitudes in case of data errors. The amount of rejected model points, because of the velocity deviation threshold (see method part in the main document), can be very different between these methods.

Figure S3: Comparison between phase-velocity maps at two selected periods from the eikonal tomography method and a linearized inversion approach.

Figure S4: Illustration of the appearance of a secondary wave front downstream from the edge of a low-velocity zone. Synthetics are calculated with a Finite Difference simulation and a source wavelet with a dominant period of 30 s. The panels at the top show the

input velocity field and three wavefield snapshots at 150, 224 and 300 s. The bottom plots illustrate the obtained waveforms (blue) at five selected locations with increasing distance to the source. The receiver numbers correspond to the numbers in the map plots. The orange dashed line shows the source waveform shifted to the approximate time of first arrival for comparison.

Figure S5: Synthetic test in which the traveltime field from a single source (red dot) to all grid points (perfect sampling) is calculated with the fast marching method (FMM). The middle panel shows the recovered velocity field after application of the eikonal tomography method and the right panel the residual between input and recovered models. White dashed lines show iso-contours of the traveltime field.

Figure S6: Synthetic test based on a finite difference (FD) simulation. The input model is identical to the one shown in Fig. S5. The source wavelet has a dominant period of 6.5 s. The panels in the middle column show the recovered velocity field without amplitude correction (top) and with amplitude correction (bottom). It can be seen that the amplitude correction significantly reduces the bias. In the upper panel, the $\lambda/2$ bias (Bodin & Maupin 2008; Lehujeur & Chevrot 2020) is clearly visible. As in Fig. S5, the sampling is 'perfect', that is there is a receiver every 3 km (minimum expected wavelength is 13 km).

Figure S7: Same as Fig. S6 but picking the traveltimes and the amplitudes from the first arrival in the time domain. This eliminates most of the bias in the first place, especially the $\lambda/2$ periodic effect is not visible anymore. However, the error in areas of a strongly distorted wavefield remain. These can be significantly reduced by the amplitude correction.

Figure S8: Same as Fig. S6, but in the FD model a source signal with a dominant period of 50 s is used. The $\lambda/2$ periodic effect is much clearer and the associated error in the phase velocities more significant. The amplitude correction very effectively removes this bias.

Figure S9: Same as Fig. S6 but for the FD model a source signal with a dominant period of 50 s is used and the traveltimes and amplitudes are picked from the first arrival in the time domain. This eliminates the $\lambda/2$ periodic bias from the phase interactions.

Figure S10: Same as Fig. 7 of the main document, but instead of a finite difference simulation, the synthetics are calculated with the FMM method so that no finite-frequency effects appear (no reflection, no secondary wave front, etc.). The bias in the recovered, anisotropic map is almost identical to the one for the FD simulation in Fig. 7 of the main document. This shows in junction with Fig. S11 that the bias is mostly caused by insufficient sampling.

Figure S11: Same as Fig. S10 but with 'perfect' sampling, that is a receiver at every point of the grid.

Figure S12: Comparison of the work of Schippkus *et al*. (2018, top), Schippkus *et al*. (2019, left) and this work (right) for the Vienna basin region. The studies of Schippkus *et al*. (2018, 2019) are based on group velocity measurements as opposed to phase velocities in this work.

Please note: Oxford University Press is not responsible for the content or functionality of any supporting materials supplied by the authors. Any queries (other than missing material) should be directed to the corresponding author for the paper.